

# Design, Control and Evaluation of a Novel Soft Evertng Robot for Colonoscopy

Jialei Shi, Korn Borvorntanajanya, *Student Member, IEEE*, Kaiwen Chen, *Member, IEEE*, Enrico Franco, and Ferdinando Rodriguez y Baena, *Member, IEEE*

**Abstract**—Colonoscopy is a medical procedure used to examine the inside of the colon for abnormalities, such as polyps or cancer. Traditionally, this is done by manually inserting a long, flexible tube called a colonoscope into the colon. However, this method can cause pain, discomfort, and even the risk of perforation. To address these shortcomings, advancements in technology are needed to develop safer, more intelligent colonoscopes. This paper presents the design, control and evaluation of a self-growing soft robotic colonoscope, leveraging the evertion principle. The device features a tube with an 18 mm diameter, constructed from stretchable fabric, which grows 1.6 m at the tip under pressurization. A pneumatically driven, elastomer-based manipulator enables omni-directional steering over 180° at the tip. An airtight base houses motors and spools that control the material and regulate growth speed. The robot operates in two modes: teleoperation via joysticks and autonomous navigation using sensor inputs, such as a tip-mounted camera. Thorough *in-vitro* experiments are conducted to assess the system's functionality and performance. Results illustrate that the robot can achieve locomotion in confined spaces such as a colon phantom, while exerting contact forces averaging less than 0.3 N. Our soft robot shows potential for improving the safety and autonomy of colonoscopies, while reducing discomfort to patients.

**Index Terms**—Soft growing robots, Evertng robots, Colonoscopy, Medical devices.

## I. INTRODUCTION

THE medical field has placed a significant emphasis on advancing the safety and autonomy of medical devices for future surgeries [1]. These advancements are driven by two key factors: artificial intelligence and disruptive hardware innovation [2]. Soft robotic medical devices, leveraging compliant and smart materials, have the potential to significantly improve safety. In this context, colonoscopy, a procedure primarily used to detect colorectal cancer, requires a new paradigm to mitigate patient discomfort, increase completion rates, and reduce the learning curve for clinicians [3], [4].

This work is supported by the Engineering and Physical Sciences Research Council, Grant EP/X033546/1, and partially supported by the InnoHK initiative of the Innovation and Technology Commission of the Hong Kong Special Administrative Region Government, Multi-Scale Medical Robotics Centre, The Chinese University of Hong Kong. (*Corresponding author: Ferdinando Rodriguez y Baena*).

Jialei Shi, Korn Borvorntanajanya, Enrico Franco and Ferdinando Rodriguez y Baena are with the Hamlyn Centre for Robotic Surgery, Department of Mechanical Engineering, Imperial College London, London, UK. (e-mail: f.rodriguez@imperial.ac.uk).

Kaiwen Chen is with the Department of Electrical and Electronic Engineering, Imperial College London, London, UK. (e-mail: kaiwen.chen16@imperial.ac.uk).

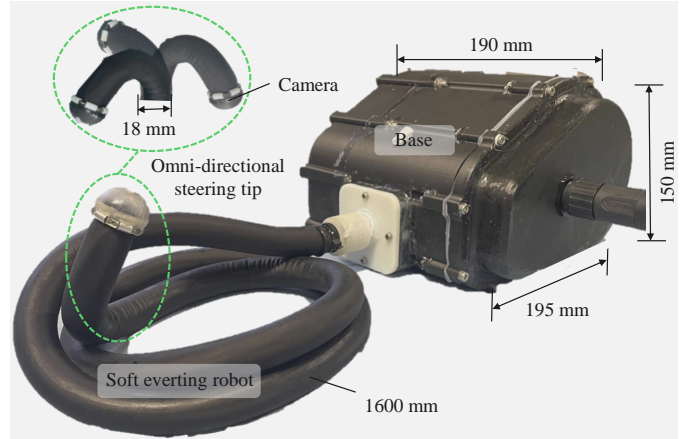


Fig. 1. Overview of the soft evertng robotic system. The robot can grow up to 1.6 m, with a tube diameter of 18 mm. A soft manipulator is embedded at the tip of the evertng structure to achieve omni-directional steering.

## A. Related Work

The fundamental principles of colonoscopy have remained unchanged for decades. A long, flexible instrument, known as colonoscope, is manually inserted into the colon through the rectum. The colonoscope is typically equipped with a camera for detecting abnormalities and channels for therapeutic instruments, such as inflation of the mesentery to facilitate navigation, or flushing fluid after a polyp excision [5]. However, inserting the colonoscope inevitably stretches the colon, leading to discomfort and, in severe cases, perforation [6]. Additionally, various loops, such as N-loops, alpha loops, or omega loops, can form during the procedure, obstructing the insertion and causing significant pain [7]. To alleviate discomfort, variable-stiffness colonoscopes have been developed, capable of stiffening the proximal 40 ~ 50 cm of the instrument [8]. However, to further alleviate patients' discomfort and pain caused by the insertion of the colonoscope, new approaches are needed to navigate the scope through the colon.

Advancing colonoscopes through the colon can be achieved using alternative methods besides traditional insertion. One common approach is to leverage peristaltic motion, inspired by the locomotion of inchworms. With this technique, the scope makes contact with the colon walls to create anchoring points. For example, in one method, two clamps located at the proximal and distal ends of a probe adhered to the colon wall using vacuum suction, while the central portion alternately elongated and contracted to move forward [9]. Similarly, a soft pneumatic robot introduced in [10] used inflatable

balloons to anchor itself, with an extensible central section for propulsion. In [3], peristaltic motion was achieved through the shape-morphing ability of a three-segment soft robot: the distal and proximal segments bent on opposite sides, forming a curved shape for anchoring, while the central segment extended or contracted to produce forward motion. Another example in [11] featured an eel-like soft robot that advanced through the colon using dynamic sinusoidal movements at varying frequencies. However, peristaltic locomotion can cause patient discomfort, as the devices must physically adhere to the colon's wall. Additionally, the deformability of the colon and the low friction of its inner surface present significant challenges for these devices. To address these limitations, more complex systems, such as magnetically actuated scopes, have been explored [4], [12]. These scopes offer several unique advantages, including reduced patient discomfort and enhanced autonomy in colonoscopy. However, they rely on external magnetic fields, which can be expensive, complex, and only available in specialized facilities, potentially limiting their accessibility. Capsule endoscopes offer another potential solution: a camera housed inside a small capsule travels through the digestive tract, capturing images as it moves [13]. However, precise motion control and therapy delivery with capsule endoscopes remain challenging.

Over the past decade, the development of soft-everters robots, also known as vine robots [14], has provided valuable insights for designing next-generation colonoscopes. These robots feature a tubular structure that grows at the tip by unfolding and rolling out stored material through internal pressurization [15], [16]. This unique mode of locomotion allows everting robots to advance without relying on anchoring points, minimizing strain on the surrounding environment. There are two primary approaches to utilizing soft-everters robots in colonoscopy. One method involves attaching a traditional colonoscope inside the inverted tube, allowing the everting tube to grow through the colon and pull the colonoscope along with it [17]. In this scenario, the everting robot serves as a protective sleeve [18], but this sacrifices the inherent compliance of soft-everters robots. Alternatively, growing robots can function as stand-alone colonoscopes. For example, in [19], a latex-based tip-extending colonoscope was developed with tubes coiled at the tip and a camera integrated for examination. However, this device lacked active tip steering. While steering of everting robots can be achieved through predefined mechanisms [20], such as pneumatic pouches [21], latches [15], tendons [22], heat-welding [23] or passive interactions with the environment [24], [25], colonoscopy demands active steering similar to that of traditional colonoscopes. A controllable and steerable tip is essential for navigating in the complex geometry of the human intestine, facilitating thorough examination while reducing patient discomfort. Existing tip-steering designs, such as rigid joints [26] or soft bending manipulators [27], [28], have been explored, though they often suffer from limited range of motion. Magnetic actuation has also been investigated for selective tip steering, using novel valves [29], tip-mounted magnets [30], or magnetic skins [31], though this approach typically requires external devices carrying or generating magnets.

## B. Contributions and Outline

While soft everting robots demonstrate great potential for developing safer, more agile, and intelligent robotic colonoscopes, a system that incorporates adequate tip steering and (semi-)autonomous locomotion capabilities has yet to be fully explored. To this end, this paper presents a soft everting robot designed for colonoscopy, encompassing the robot's design, control, and *in-vitro* evaluation. The key contributions of this work include the following points.

- A soft everting robotic system for colonoscopy is devised and evaluated (see Fig. 4). The robot features an 18 mm compliant tube structure and active omni-directional tip steering of over 180°. Its performance and suitability for colonoscopy are thoroughly evaluated *in-vitro*, via locomotion in soft and rigid phantoms (see Section V-A), measurement of contact forces and shape-holding in constrained spaces (see Section V-B).
- A control pipeline is proposed and validated, demonstrating that the soft robotic device can operate in both teleoperation mode using a joystick and in autonomous-locomotion mode based on sensor inputs. In autonomous-locomotion mode, the robot can either follow predefined paths by employing a closed-loop adaptive controller or navigate inside an unknown environment, represented by a soft colon phantom, via image-guidance using a tip-mounted camera (see Sections V-C and V-D). To the best of the authors' knowledge, this is the first example of autonomous navigation with a soft everting robot for colonoscopy.

The rest of this paper is organized as follows: Section II details the hardware design, fabrication and system integration of the developed robot. The characterization of the growth speed and tip steering mechanism of the robot is in Section III. Section IV outlines the control pipeline, supporting the robot to operate in teleoperated and autonomous modes, followed by *in-vitro* experimental evaluation in Section V. Section VI discusses the experimental evaluation results of the system and identifies future research. Section VII concludes this work.

## II. HARDWARE DESIGN, FABRICATION, AND SYSTEM INTEGRATION

This section starts by outlining the key requirements for robotic colonoscopes, followed by the fabrication of the soft everting tube structure, design details of the tip steering mechanism, and the system integration.

### A. Medical Requirements

Several requirements need to be considered for robotic colonoscopes. The average diameters of the distal and proximal colon are 31 mm and 42 mm, respectively. The proximal colon is defined from the cecum to the splenic flexure, and the remainder is the distal colon [32]. The robot diameter should be smaller than these values. In addition, the outer casting of colonoscopes is made of plastic, their flexural rigidity depends on diameters and might vary along their length, e.g., between 160 to 240 Ncm<sup>2</sup>, see [33]. In principle, more compliant

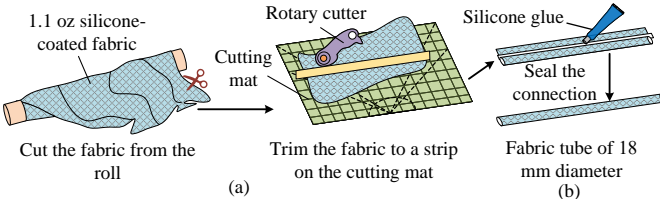


Fig. 2. Fabrication process of the soft evertng structure, consisting of two steps (a) cutting, trimming and (b) gluing the nylon ripstop fabric.

structures can reduce flexural rigidity and thus mitigate contact forces with the colon. Moreover, the anatomy of the colon has various bends, e.g., an S shape of the sigmoid colon. The robotic device should be able to generate sufficient steering angle to pass these bends.

According to above facts and dimensions from existing colonoscopy devices [5], key characteristics of colonoscopes are: (1) a 1.6 ~ 1.7 m long flexible structure, with preferable outer diameter of less than 18 mm; (2) a steerable omnidirectional tip, with steering angles of  $160^\circ \sim 180^\circ$ ; (3) working channels to carry tools, such as light, camera, suction drain, CO<sub>2</sub> insufflation, and water flush.

### B. Fabrication of the Soft Evertng Structure

The soft evertng structure is made of silicone coated ripstop nylon fabric [1.1 oz Silnylon, Ripstop by the Roll]. This fabric is highly compliant and coated with a silicone/Polyurethane layer on each side. The fabrication process of the evertng structure follows [34] and is illustrated in Fig. 2. First, a piece of fabric is placed on a cutting mat, where the warp and weft threads of the fabric are aligned with the  $45^\circ$  line of the cutting mat (see Fig. 2(a)). A rotary cutter is employed to cut a strip of fabric with a width of 60 mm and a length of 1600 mm. Second, a thin layer of silicone adhesive [Sil-Poxy, Smooth-On] is placed on the double-sided tape along the middle of the fabric. Two edges of the fabric strip are then folded over so that they overlap by 2 mm, as shown in Fig. 2(b). As a result, the area is glued by the silicone adhesive, and a fabric tube with a diameter of 18 mm is formed. Please note that the fabric tube folds as the robot grows, so two fabric tubes need to be connected using the silicone adhesive to achieve a growth length of 1600 mm.

### C. Design and Fabrication of the Steerable Tip Mechanism

The steering of the evertng robot is achieved by a tip mechanism that comprises a pneumatic-driven soft manipulator and an interlock tip structure, as illustrated in Fig. 3(a). Specifically, the soft manipulator is exclusively made of a compliant elastomer with nine actuation chambers and a free central lumen for the evertng material. To achieve an omnidirectional steering, adjacent actuation chambers are internally connected together in groups of three. To keep the soft steering manipulator always at the tip of the evertng structure and reserve spaces for mounting cameras, an interlock mechanism is designed (see Fig. 3(a)). The interlock mechanism is made of six roller sets, with inner rollers attached at the tip of the

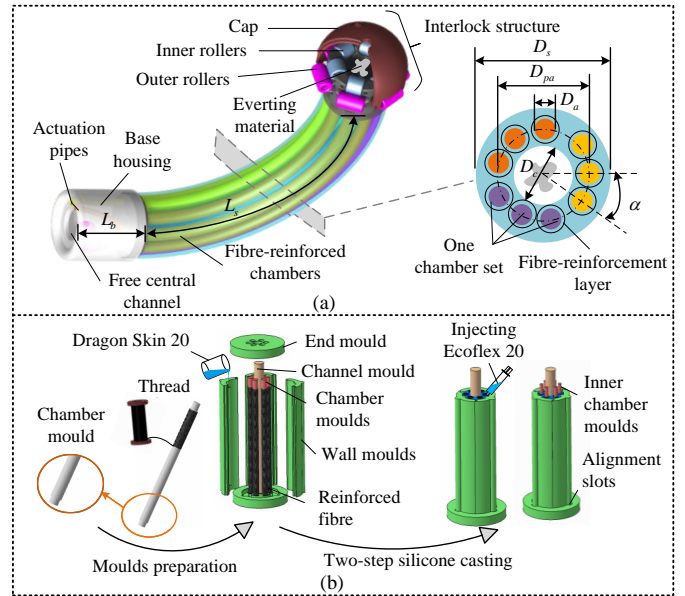


Fig. 3. (a) Assembly of the tip steering mechanism, including the soft steering manipulator and interlock mechanism. (b) Fabrication of the soft steering manipulator. Main dimensions are listed in Table I.

steering manipulator and outer rollers mounted at the cap. All rollers have embedded bearings to minimize friction. A small gap between the inner and outer rollers allows the evertng material to pass. Compared to the tip mount reported in [35], our design has increased roller sets while achieving a smaller size. Additional, our tip mount uniquely interlocks with the tip steering manipulator, allowing our robot to grow with large omni-directional steering angles.

Fig. 3(b)) illustrates the fabrication process of the steering manipulator. First, the reinforcement layer is formed by wrapping in-extensible thread to nine circular chamber molds [36], [37]. All the molds are then assembled before pouring silicone [Dragon Skin 20, Smooth-On]. Silicone cures at  $60^\circ\text{C}$  in a heating oven. After that, the reinforcement thread is sealed via a thin silicone layer with a thickness of 0.5 mm. This silicone layer is made by injecting silicone [Ecoflex 20, Smooth-On] in the gap between inner chamber molds and thread. Top and bottom sides are then sealed using silicone adhesive [Sil-Poxy, Smooth-On]. The main dimensions of the steerable tip mechanism are summarized in Table I.

TABLE I  
MAIN DIMENSIONS OF THE STEERABLE TIP MECHANISM (SEE FIG. 3(A))

Symbol	Description	Dimension
$L_s$	Length of the soft manipulator	105.0 mm
$L_b$	Length of the base housing	25.0 mm
$D_a$	Diameter of the actuation chamber	2.5 mm
$D_s$	Diameter of the manipulator	16.9 mm
$D_{pa}$	Diameter of circular pattern of the chambers	12.5 mm
$D_c$	Diameter of the central lumen	7.9 mm
$\alpha$	Angle between adjacent chambers	40 degrees

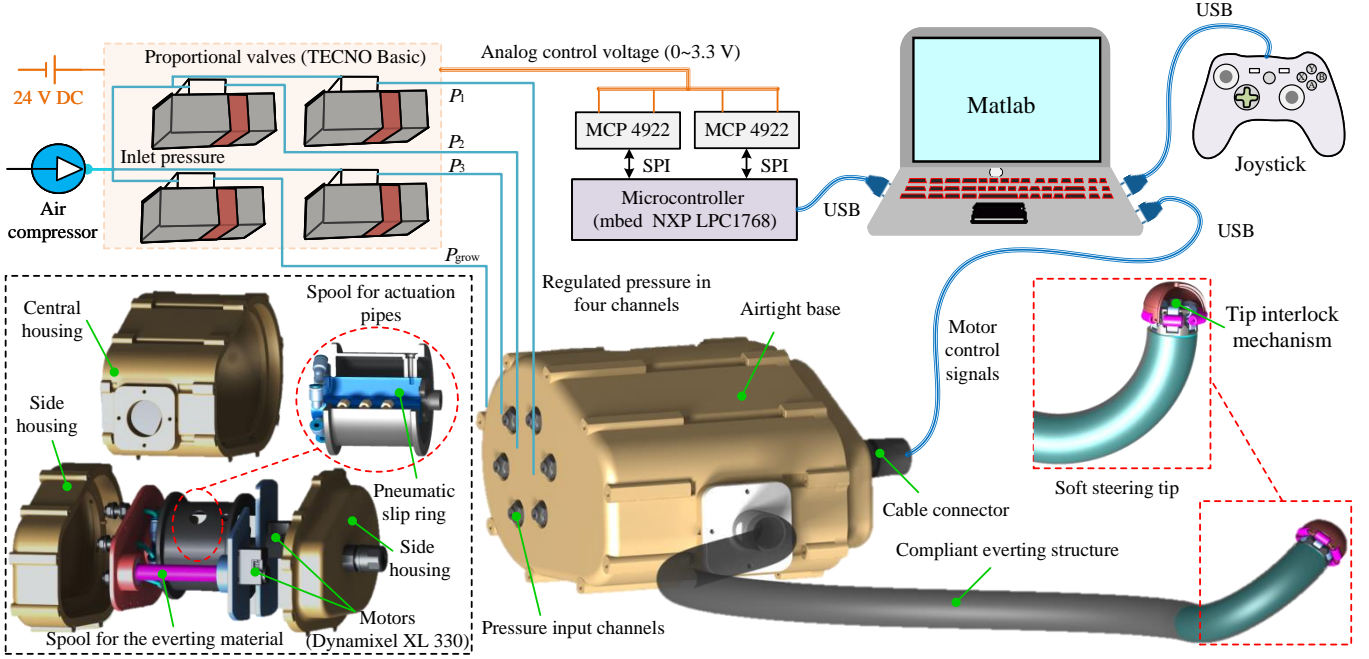


Fig. 4. Overview of the system. The bottom-right section illustrates the soft evertng robot, featuring a tip-steerable growing structure and an airtight base. The base houses two motorized spools for evertng material and actuation pipes, as detailed in the bottom-left section. The top section presents the control system, where a laptop communicates with a microcontroller to drive four proportional valves, enabling control of the robot's steering and growth. Meanwhile, a joystick provides user input to define specific steering and growth commands.

#### D. System Integration

Fig. 4 shows the integrated soft evertng robotic system. To store the evertng material and actuation pipes for the steerable tip manipulator, two motorized spools [XC330-T288-T, Dynamixel] are integrated in an airtight base. The spool for the actuation pipes is made of a 6-in-6-out pneumatic slip ring, and the slip ring prevents actuation pipes from getting tangled when the spool rotates. Four proportional pneumatic valves [TeCNO Basic, Hoergiber] regulate three pressure channels for the steerable manipulator (i.e.,  $P_1 \sim P_3$ ) and one growth pressure for the evertng structure (i.e.,  $P_{\text{grow}}$ ). These valves are controlled by analogue signals from DAC boards [MCP 4922, Microchip], communicating with a microcontroller [NXP LPC1768, Mbed] via SPI bus. The growth pressure is monitored by an external sensor [4525DO, TE Connectivity]. A joystick [Xbox 360, Microsoft] can be used to set the growing and steering motions of the evertng robot in the teleoperation mode. The tip position and orientation of the evertng robot can be measured with an electro-magnetic (EM) sensor (Aurora, NDI) in laboratory tests. All components communicate with Matlab R2024a via serial links.

### III. CHARACTERIZATION OF THE SOFT EVERTING ROBOT

This section experimentally characterizes key performances of the soft evertng robot, including the growth speed at different pressure, steering capability and maximum forces generated by the tip steering mechanism.

#### A. Growth Speed

To effectively navigate within the colon, a confined 3D environment, the robot should be able to grow in both vertical

and horizontal directions. Therefore, the vertical and horizontal growth speeds of the soft evertng robot are measured under various pressures. To this end, an acrylic tube with an inner diameter of 36 mm is positioned either vertically or horizontally, creating a straight, restricted pathway (see Fig. 5). According to [15], the straight growth speed  $v$  of evertng robots can be described by

$$v = a(P_{\text{grow}} - P_m)^b, \quad (1)$$

where  $a$  and  $b$  are constants, while  $P_{\text{grow}}$  and  $P_m$  are the applied pressure in the fabric tube and the minimum pressure required for growth, respectively. In this set of experiments, the steering pressure remains zero to achieve a straight motion. The pressure for the evertng structure ranges between 0 ~ 15 kPa and each value is applied for 3 seconds, while each trial repeated three times.

Fig. 5 illustrates that the averaged maximum vertical and horizontal growth speed is 158.2 mm/s and 308.9 mm/s, respectively. Moreover, Fig. 5 shows that the experimental data agrees with (1), with R-squared values over 0.99. In particular, the values of  $a$  for horizontal and vertical motion are 34.47 and 16.83, respectively. The corresponding values of  $b$  are 0.91 and 1.10, respectively. The minimum required growth pressure  $P_m$  for horizontal and vertical motion is 3.8 kPa and 7.4 kPa, respectively. In general, the vertical growth speed is about 50% of the horizontal growth speed at a same pressure. This is primarily due to the weight of the soft manipulator and of the tip interlock structure (see Fig. 3(a)).

#### B. Steering Angle

The steering angle of the evertng robot depends on both the steering pressure and the growth pressure. To characterize

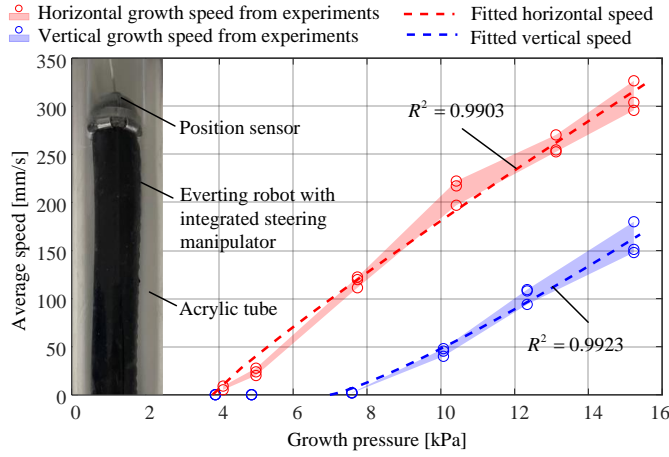


Fig. 5. Characterization results for the horizontal and vertical growth speed when different pressure is applied to the evertting structure. The tip steering manipulator is not actuated.

the steering capability, the growth pressure was set between  $0 \sim 15$  kPa, with an interval of 5 kPa. At each growth pressure, the steering pressure continuously increased from 0 to 300 kPa in 30 seconds. The steering manipulator has three sets of actuation chambers (see Fig. 3(a)). As such, the steering pressure of the tip manipulator was applied to either one chamber set or two chamber sets to generate steering motions, and each test was repeated three times.

Fig. 6 shows the linearly interpolated map of the steering angle at different growth and steering pressure. The results indicate that the steering angle with two actuated chamber sets is larger than that with one chamber set, subject to the same steering and growth pressure. The maximum steering angle with either two chamber sets or one chamber set is  $201.8^\circ$  and  $173.9^\circ$ , respectively. These angles are achieved when the growth pressure is zero and the steering pressure is 300 kPa. In general, the steering angle decreases with the growth pressure. For instance, the maximum steering angle with two chamber sets and one chamber set decreases to  $155.9^\circ$  and  $138.0^\circ$  when the growth pressure is 15 kPa. This occurs since a larger growth pressure increases the flexural stiffness of the evertting tube structure. It is noteworthy that a minimum steering pressure of about  $20 \sim 35$  kPa is required to generate a steering motion. This might be due to the dead-zone of the pressure regulators and friction between the steering mechanism and the fabric tube.

### C. Maximum Tip Force of the Steering Mechanism

The maximum generated force from the soft steering manipulator is characterized. In the experiment, the robot was initially positioned horizontally, with its tip locally constrained by a force sensor [Gamma, ATI]. As the robot steers toward the sensor, its tip is allowed to slide along the sensor's surface. This setup ensures that the force generated by the robot is directed perpendicularly to the sensor, allowing for accurate measurement of the maximum force. In this case, the final tip orientation of the robot does not need to be considered. Meanwhile, a fixed base is employed to constrain the tail

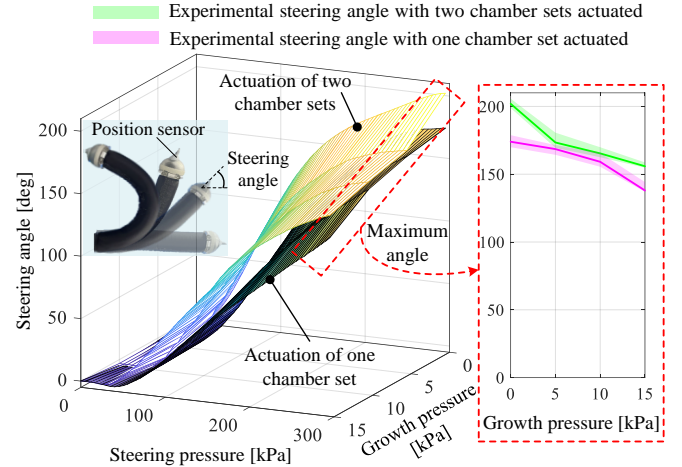


Fig. 6. Characterization results for the tip steering angle of the evertting robot when different steering pressure ( $0 \sim 300$  kPa) and growth pressure ( $0 \sim 15$  kPa) are applied.

of the inner steering manipulator, see Fig. 7. In tests, the steering pressure is set as the maximum value of 300 kPa, while the growth pressure increases from 0 kPa to 15 kPa with an interval of 5 kPa. The generated force is measured when either one chamber set or two chamber sets of the manipulator are actuated, and each test is repeated three times.

Fig. 7 shows that the maximum generated forces range between  $0.47 \sim 0.72$  N when the steering pressure is 300 kPa. On average, the tip forces with two chamber sets are slightly higher (about 0.02 N) than those with one chamber set. In addition, the tip force increases with the growth pressure. For instance, the average force increases by 0.1 N when the growth pressure varies from 0 kPa to 15 kPa. A higher stiffness of the pressurized evertting structure might contribute to a higher tip force.

## IV. CONTROL OF THE SOFT EVERTING ROBOT IN CONSTRAINED ENVIRONMENTS

Levels of autonomy for medical robots are defined in [1], from no autonomy to full automation. To demonstrate the developed system can support different levels of autonomy, this section presents a set of control algorithms to operate the robotic system in two modes: teleoperation mode controlled by human via joysticks and autonomous control from exteroceptive information, e.g., images from cameras. The control pipeline is illustrated in Fig. 8.

### A. Low-level Motion Control

In the teleoperation mode, the joystick is employed to set the growth speed and steering angle of the robot. As such, this section details the low-level motion control.

1) *Growing Motion:* The robot growing motion is actuated by two motorized spools. To achieve the growing motion, the housing base needs to be pressurized first and the fabric material stored on the spool then needs to be released. Meanwhile, the actuation pipes for the steerable tip manipulator have to be released. It is noteworthy that the speed of released fabric

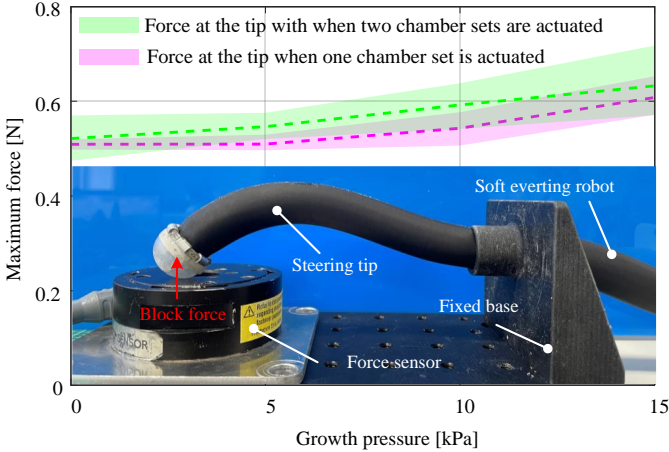


Fig. 7. Characterization results for the maximum force generated by the tip steering manipulator when one chamber set and two chamber sets are actuated by 300 kPa.

material moves at twice the speed of the robot tip, as the fabric folds during the evert process. As such,

$$\omega_1 = \frac{2r_2}{r_1\eta} \omega_2, \quad P_{\text{grow}} > P_m, \quad (2)$$

where  $\omega_1$  and  $\omega_2$  are the speed of the spool for the fabric and actuation pipes, respectively.  $r_1$  and  $r_2$  are the radii of these two spools, while  $\eta$  is the contraction ratio of the fabric tube subject to pressurization. By controlling the speed of  $\omega_1$  and  $\omega_2$ , the growing speed of the robot can be adjusted accordingly at different growth pressures  $P_{\text{grow}}$ .

2) *Steering Motion*: The steering manipulator can bend with two degrees of freedom, described by a set of two steering coordinates  $(q, \phi)$  in the body frame, where  $q$  is the steering angle and  $\phi$  is the orientation of the steering plane, indicated in Fig. 8. The relation between the steering coordinates, the steering direction command  $P_{\text{steer}} \triangleq [P_x, P_y]^T$  and the growth pressure  $P_{\text{grow}}$  is

$$q = \sigma(|P_{\text{steer}}|, P_{\text{grow}}), \quad (3a)$$

$$\phi = \angle(P_{\text{steer}}), \quad (3b)$$

where  $\sigma(\cdot, \cdot)$  is the pressure-steering characteristic mapping reported in Fig. 6, and  $\angle(\cdot)$  denotes the angle between the a vector and the positive  $x$ -axis (see Fig. 8).  $P_{\text{steer}}$  is the steering direction command (left, right, up and down). In the teleoperation mode,  $P_{\text{steer}}$  is from the joystick, as reported in Fig. 6.

Key to the steering control is to calculate the actuation pressures of the tip steering manipulator  $P_{\text{act}} = [P_1 \ P_2 \ P_3]$  from the steering direction command  $P_{\text{steer}} = [P_x \ P_y]$ , which can be solved by

$$\begin{bmatrix} P_x \\ P_y \end{bmatrix} = \underbrace{\begin{bmatrix} 0 & \frac{\sqrt{3}}{2} & -\frac{\sqrt{3}}{2} \\ -1 & \frac{1}{2} & \frac{1}{2} \end{bmatrix}}_{\triangleq T} \begin{bmatrix} P_1 \\ P_2 \\ P_3 \end{bmatrix}. \quad (4)$$

All solutions to the under-determined system (4) can be expressed as  $P_{\text{act}} = T^+ P_{\text{steer}} + [1, 1, 1]^T c$ , where  $T^+ \triangleq$

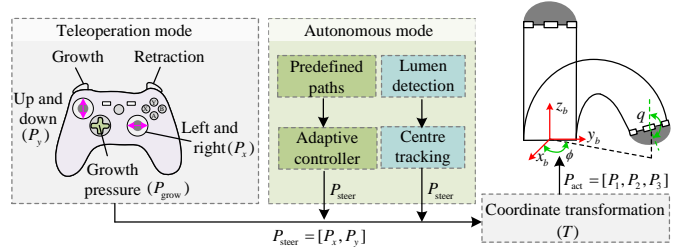


Fig. 8. Control diagram of the system, including teleoperation mode and the autonomous mode.  $\{x_b, y_b, z_b\}$  is the body frame at the base of the steering manipulator.

$T^\top (TT^\top)^{-1}$  is the Moore-Penrose inverse of  $T$  and  $c$  is an arbitrary real number. Since the actuation pressure allowed in each chamber is between 0 to  $P_{\max} = 300$  kPa, a viable actuation pressure  $\bar{P}_{\text{act}}$  is computed as

$$\hat{P}_{\text{act}} = T^+ P_{\text{steer}} - [1, 1, 1]^T \min(T^+ P_{\text{steer}}), \quad (5a)$$

$$\bar{P}_{\text{act}} = \frac{\min\left(\left[P_{\max}, \max(\hat{P}_{\text{act}})\right]^\top\right)}{\max(\hat{P}_{\text{act}})} \hat{P}_{\text{act}}, \quad (5b)$$

where  $\max(\cdot)$  and  $\min(\cdot)$  denote the maximum and minimum element of a vector, respectively. Equation (5a) is a particular solution to (4) with the minimum chamber pressure being 0 and (5b) is a saturated actuation pressure vector with its maximum chamber pressure saturated at  $P_{\max}$ . Note that the normalized actuation pressure vector  $\bar{P}_{\text{act}}$  is a vector of positive values multiple of  $\hat{P}_{\text{act}}$  and by linearity, the resulting saturated steering pressure  $\bar{P}_{\text{steer}} \triangleq T \bar{P}_{\text{act}}$  is a vector of positive values multiple of the original  $P_{\text{steer}}$ . Therefore, the saturation introduced by (5b) preserves the direction of the steering and the steering plane: only the maximum steering angle is restricted. Our steering control method has two distinctive features. First, steering and growth control are decoupled in our approach, eliminating the need to compute the full robot's Jacobian matrix  $J \in \mathbb{R}^{6 \times 4}$ , which is required in [21]. Second, our approach enables calculating actuation pressure in one step by solving linear equations, while satisfying their maximum limits (see (5b)). In contrast, the steering control in [14] relies on a multi-step iterative approach to obtain desired actuation pressure.

When operating in the teleoperation mode, commands from the joystick directly set the growth speed via (2) and the steering motions via (4) as illustrated in Fig. 8. This low-level control also lays the foundation for the autonomous control described in the next section.

### B. High-level Autonomous Locomotion Control

1) *Predefined path-following*: To highlight that the robotic system can support autonomous navigation, an adaptive path-following controller is first presented. The path-following problem of the robotic colonoscope along a predefined trajectory can be recast into the problem presented in [38]. In this case, the locomotion of the soft evert robot is decomposed into two components: the constant speed advancing along the

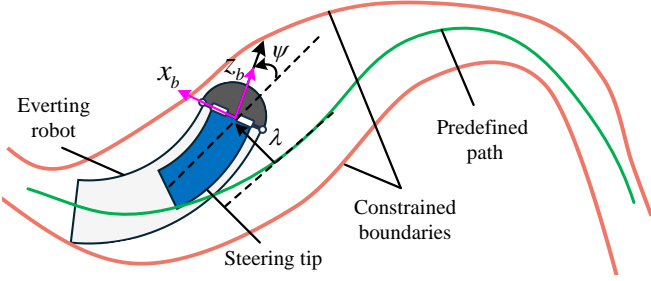


Fig. 9. Illustration of predefined path-following control when the soft evertng robot advances in constrained spaces.

trajectory (realised by a constant-rate spool rotation), and the steering on the steering plane (see Fig. 9). The associated kinematic model is described by

$$\dot{\lambda} = v \sin(\psi), \quad (6a)$$

$$\dot{\psi} = -\frac{\kappa}{1-\kappa\lambda} v \cos(\psi) + \omega, \quad (6b)$$

where  $\lambda$  and  $\psi$  are the lateral deviation and orientation deviation from the predefined path, respectively, and both can be measured in real time;  $v$  is the growth speed;  $\kappa$  is the curvature of the predefined path at the current location; and  $\omega$  is the angular rate of the steering action, which is used as a control input.

To simplify the problem, we consider the case in which  $\psi \ll 1$  and  $\lambda \ll 1/\kappa \triangleq R$ , where  $R$  is the radius of curvature of the predefined path. These allow the approximations that  $\sin(\psi) \approx \psi$  and  $\frac{1}{1-\kappa\lambda} \approx 1 + \kappa\lambda$ .  $v$  is a known constant (determined by the angular rate of the spool). The system can then be re-written using the equations

$$\dot{e}_1 = e_2, \quad (7a)$$

$$\dot{e}_2 = \varphi^\top(x)\theta + u, \quad (7b)$$

where  $e_1 \triangleq \lambda$ ;  $e_2 \triangleq v\psi$ ;  $u \triangleq v\omega$ ;  $\theta \triangleq [-\kappa v^2, -\kappa^2 v^2]^\top$ ;  $\varphi(e) \triangleq [\cos(e_2/v), e_1 \cos(e_2/v)]^\top$ .

Note that the steering direction command  $P_{\text{steer}}$  is directly controlled, but one can indirectly control  $\omega$  by controlling the variation rate of  $P_{\text{steer}}$ . The body reference frame  $\{x_b, y_b, z_b\}$  in Fig. 8 is set up in the constrained environment (see Fig. 9) as follows. Specifically, when  $\lambda = 0$  and  $\psi = 0$ ,  $x_b$  points to the left of the predefined path and  $z_b$  points forward along the path. When the predefined path is within a plane,  $P_y = 0$  and  $P_{\text{grow}}$  is set to an appropriate constant pressure higher than  $P_m$ .  $P_x$  is then dynamically updated by

$$\dot{P}_x = \left( \frac{\partial \sigma}{\partial x_1}(P_x, P_{\text{grow}}) \right)^{-1} \omega, \quad (8)$$

where  $\frac{\partial \sigma}{\partial x_1}$  denotes the partial derivative with respect to the first argument of the function  $\sigma$ , which is non-zero within the operating range due to Fig. 6. In practice, the partial derivative can be replaced by a properly selected constant (an “average” of the value of the partial derivative) if  $\sigma$  is sufficiently “flat”, which is the case in Fig. 6. Such discrepancy can be compensated by feedback control.

Since the curvature  $\kappa$  is in general unknown and varying in practice, one cannot directly design a static feedback controller

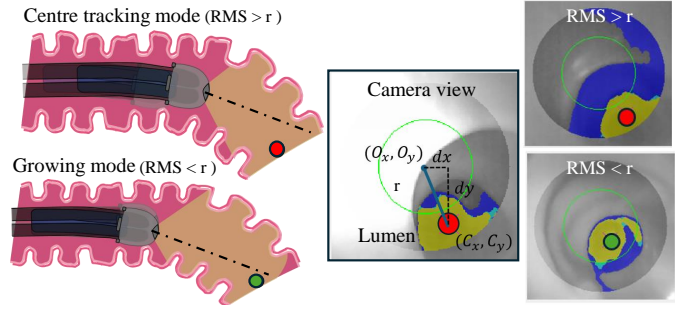


Fig. 10. Illustration of the lumen detection using the Shape from Shading technique; illustration of center tracking-mode and growth mode.

based on the tracking error model (7a). Instead, a dynamic controller that learns the unknown parameter  $\theta$  online, namely an adaptive control can be employed for this purpose. The adaptive controller for the path-following task is defined by

$$\dot{\hat{\theta}} = \Gamma \varphi(e) b^\top H e, \quad (9a)$$

$$u = -k^\top e - \varphi^\top(e) \hat{\theta}, \quad (9b)$$

where  $\hat{\theta} \triangleq [\hat{\theta}_1, \hat{\theta}_2]^\top$  is the “learned” parameter vector to replace the unknown  $\theta$ ;  $\Gamma$  is a positive definite matrix used for tuning the “learning” rate;  $b \triangleq [0, 1]^\top$ ;  $e \triangleq [e_1, e_2]^\top$ ;  $k \triangleq \frac{1}{2}\gamma^{-1}Hb$  is the vector of feedback gains; and  $H$  is a positive definite matrix that solves the following algebraic Riccati equation

$$A^\top H + HA - \gamma^{-1} Hbb^\top H + Q = 0, \quad (10)$$

with  $A \triangleq \begin{bmatrix} 0 & 1 \\ 0 & 0 \end{bmatrix}$ , and user-selected parameters  $\gamma > 0$  and  $Q = Q^\top > 0$ .

In the experiments, all integrators involved in the control algorithm are discretised by the trapezoidal rule and implemented with anti-windup saturation.

2) *Vision-based navigation control:* In clinical applications, the colon structure is unknown and the locomotion of the robot should rely on the endoscopic camera view. In this section, a vision-based navigation control approach is demonstrated.

*Lumen detection.* This step is accomplished using the Shape from Shading (SfS) technique [39], which assumes that the darkest area in the scene corresponds to the lumen. The color images captured by the camera are first converted to grayscale. These grayscale images are then transformed into a histogram model and analyzed using k-means clustering to differentiate the images into intensity layers. The number of clusters  $K$  is adaptively determined using a filtering method based on the histogram’s intensity distribution. First, the original histogram  $H(I)$  is smoothed to reduce noise using a convolution with a Gaussian kernel. Local peaks in  $H(I)$ , denoted  $I_{p,k}$  (with  $k$  indexing the peaks), serve as candidate cluster centers. The intensity difference between consecutive peaks is computed as  $\Delta I_k = I_{p,k+1} - I_{p,k}$ . An adaptive threshold is defined by  $T = \alpha(I_{\max} - I_{\min})$ ,  $0 < \alpha < 1$ , where  $I_{\max}$  and  $I_{\min}$  are the maximum and minimum intensities in the histogram. Peaks with  $\Delta I_k < T$  are merged, thus the number of distinct clusters  $K$  is adaptively determined. This approach focuses on

intensity differences rather than spatial or shape information. In this framework, the two darkest intensity layers are selected as the target lumen for navigation, as illustrated in Fig. 10. The coordinates of the center pixels representing the lumen are calculated with the centroid function

$$C_x = \frac{\sum m_x}{N_x}, C_y = \frac{\sum m_y}{N_y}, \quad (11)$$

where  $C_x, C_y$  are the  $x$ - and  $y$ -coordinates of centroid, respectively, the coordinates of the lumen are denoted by  $m$ , while its area is  $N$ .

*Locomotion control.* This is accomplished by using the center tracking concept. The lumen coordinates are subtracted from the center coordinates of the field of view ( $O_x, O_y$ ) to compute the error  $(dx, dy)$  in image plane (see Fig. 10). The Root Mean Square (RMS) of  $(dx, dy)$  is used to activated either the center-tracking mode or the growing mode.

As illustrated in Fig. 10, if the RMS error exceeds  $r$ , represented by the radius  $r$  of a specified green circle, the center-tracking mode is activated. This indicates misalignment between the lumen and the center of the field of view, thus steering is readjusted in order to recenter the lumen. In the center-tracking mode, the tip steering actuation pressure is computed from (4). To this end, an integral control algorithm is employed to compensate the error in the image plane by adjusting the steering direction command  $P_{\text{steer}}$ , which yields

$$P_{\text{steer}}^t = P_{\text{steer}}^{t-1} + k_i [dx, dy]^\top, \quad (12)$$

where  $t$  is the time step of the control loop, and  $k_i$  denotes the proportional control gain. In this mode,  $P_{\text{grow}}$  is maintained at a constant value, while both  $\omega_1$  and  $\omega_2$  are set to zero.

Conversely, if the RMS error falls below a defined threshold, the growing mode is activated. In this mode, it is assumed that the lumen is sufficiently aligned with the tip of the evertng robot, therefore the robot grows with a desired tip steering angle. To this end, the steering pressure remains constant with  $P_{\text{grow}}$  set above  $P_m$ , and the velocities of the spools are fixed at constant values.

Similar to [15], [21], our visual servoing employs an eye-in-hand control approach, where the camera is mounted on the robot's growing tip. In contrast to eye-to-hand control, where the camera remains fixed in the environment and observes the robot from an external viewpoint [40], eye-in-hand control is more suitable for confined or dynamic environments, such as the colon. Our steering controller adopts a rule-based approach that adaptively aligns the image center with the detected lumen via the SfS technique, without relying on predefined image features, such as designated objectives required in [21]. Unlike the proportional controller used in [40] for tracking predefined trajectories, our controller keeps the robot's tip within the detected lumen area in an unstructured colon.

## V. EXPERIMENTAL VALIDATION AND EVALUATION

This section presents the experimental validation and evaluation of the robotic system: Experiment 1 validates the robot locomotion in soft and rigid phantoms when it is teleoperated by a joystick; Experiment 2 investigates the robot's shape-holding capability and contact forces between the robot and the

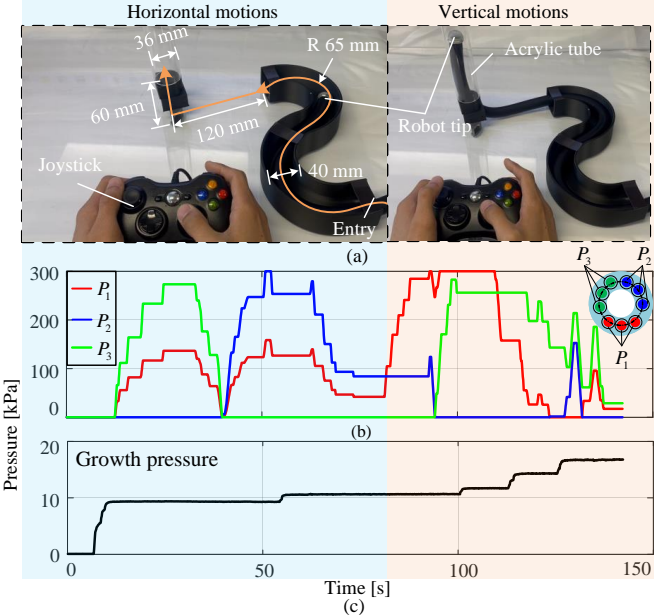


Fig. 11. Results for Experiment 1 - Teleoperated navigation in a rigid phantom. (a) Experimental setup. (b) The applied actuation pressure  $P_1, P_2, P_3$  (defined in Eq. (4)) of the tip steering manipulator and (c) the growth pressure during the test.

environment during locomotion; Experiments 3 and 4 illustrate the autonomous control mode in two cases, i.e., predefined path-following and vision-based navigation, respectively.

### A. Experiment 1: Locomotion in Rigid and Soft Phantoms

1) *Protocol:* The robot was controlled with the joystick to move inside two different phantoms. i) In the first test, the robot navigated a phantom consisting of a planar S shape followed by a vertical acrylic tube. The robot required both planar and vertical motions to navigate in this phantom. Detailed dimensions of the rigid phantom are reported in Fig. 11(a). ii) In the second test, the robot navigated in a soft collapsed phantom made of nylon fabrics. The phantom has an overall length of 1.2 m and a diameter of 40 mm. The phantom was loosely fixed by four points, as shown in Fig. 12. During above two tests, the user directly observed the robot's tip position within the phantom throughout the operation. iii) In the third test, the robot navigated a soft colon phantom [AK107, Adam, Rouilly]. The user operated a joystick relying on image guidance from the on-board camera [MD-V1000LH-120, MISUMI] mounted at the tip of the robot. The exact tip position of the robot is unknown. This setup mimics real-world colonoscopy procedures, where clinicians primarily use camera feedback to manipulate the scope. In all tests, the motor speed  $\omega_1$  was set to 30 RPM when the robot grows.

2) *Results:* Fig. 11(a) shows that the robot can be teleoperated to pass through the S shape rigid phantom and then steer upwards into the vertical acrylic tube. Fig. 11(b) shows the steering pressure. Specifically, the steering pressure remains below the system's maximum operating pressure of 300 kPa. Higher steering pressure is required when the robot navigates sharp turns. For example, the steering pressure reaches 300 kPa

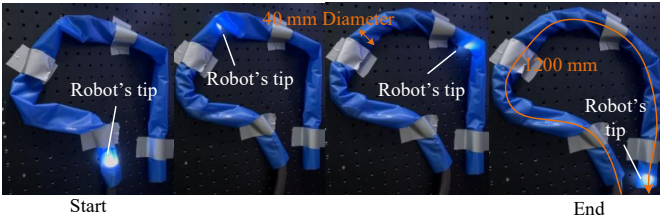


Fig. 12. Results for Experiment 1 - Teleoperated navigation in a soft collapsed colon phantom made of nylon fabrics.

as the robot moves from the first bend to the second bend of the S-shaped phantom and enters the vertical tube. Likewise, the growth pressure also increases when the robot transitions from the horizontal path to the vertical path. The growth pressure for the horizontal and vertical motions is  $10 \sim 11$  kPa and  $11 \sim 17$  kPa, respectively.

Fig. 12 demonstrates that the robot can successfully pass the collapsed phantom. Fig. 13(a) shows the dimensions of the soft colon phantom, with images captured by the tip camera during one trial. Results confirm that the robot can travel through the whole phantom (i.e., approximately 830 mm in 210 seconds) with image feedback. Figs. 13(b)-(c) show the steering and the growth pressure in one trial, respectively: the steering pressure continuously adjusts in order to keep the robot in the center of the colon, while the growth pressure is  $11 \sim 17$  kPa. Supplementary Video reports the robot advances in both rigid and soft phantoms.

### B. Experiment 2 - Contact Forces with the Environment

**1) Protocol:** The contact force between the robot and the environment was measured in three sets of tests. In the first test, the evertting robot was constrained at five points (A, B, C, D, E) to form either an S shape, a loop shape, or a U shape (see Fig. 14(a)). These shapes and their size are representative of the human colon [41] (e.g., the sigmoid colon usually has an S shape). The required force at each position to maintain the shape was measured with a force sensor.

In the second test, the robot was controlled with the joystick to pass through a phantom comprising two rigid corners connected by a plastic tube (see Fig. 15(a)). The motor speed  $\omega_1$  was 30 RPM when the growth was enabled. Two force sensors [Gamma and NANO 17, ATI] were attached to each rigid corner to measure the dynamic contact forces between the robot and phantom. Please note that forces acting on different parts of the system influence the sensor measurements. Our sensors can measure forces in all three Cartesian coordinates ( $x, y, z$ ). In this case, the measured forces are transmitted from contact points between the robot and the phantom, and the overall contact force is computed as the vector sum of the measured forces in all three directions. Before each trial, the sensor was calibrated by zeroing the sensors to ensure accurate force measurements. Each test was repeated three trials.

The third test further investigated the comparisons of interaction forces between the evertting robot and a conventional colonoscope [Olympus CF-H260AZL], both operated by the same colonoscopist. The setup is similar to that of the second

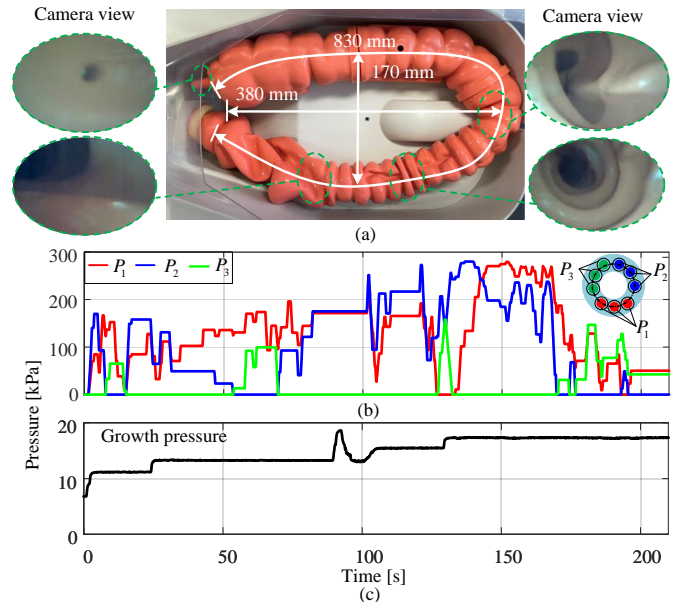


Fig. 13. Results for Experiment 1 - Teleoperated navigation in a soft colon phantom. (a) Experimental setup. (b) The steering pressure of the tip manipulator and (c) the growth pressure in one trial.

trial, as detailed in Fig. 16(a), which represents a section of the human sigmoid colon. The colonoscopist operated the robot and the colonoscope to pass the rigid phantom, exclusively guided by the tip-mounted camera. Two force sensors recorded contact forces during the whole process. After the test, the colonoscopist filled out the NASA Task Load Index (NASA-TLX) form (0 ~ 100 scores) to subjectively assess the perceived workload associated with the two devices. Please note that the colonoscopist had one trial to be familiar with operating the robot prior to the test.

**2) Results.:** Fig. 14 shows the measured forces at each of the five points when different growth pressures are applied to the fabric tube. Fig. 14(b) illustrates that the contact force increases with a higher growth pressure. When the growth pressure is 15 kPa, the maximum required force is 0.57 N, 0.44 N and 0.34 N for the S shape, the loop shape and the U shape, respectively. In most cases, the maximum forces are lower than 0.4 N to hold robot's shapes.

Figs. 15(b)–(e) show the results when the robot is teleoperated to pass through the phantom in Fig. 15(a). In one trial, Figs. 15(b) illustrates that the maximum forces are lower than 0.6 N. During 0 ~ 16 s, the robot tip is within the first rigid corner, and  $f_2$  remains zero. The robot passes the plastic tube during 23 ~ 32 s and  $f_2$  starts to increase. From 32 s, the tip is controlled to enter the second rigid corner (see Fig. 15(a)), and  $P_1$  and  $P_3$  increase to 300 kPa. The robot navigates the second corner after 62 s, when the forces reach their peak values. During the whole test, the growth pressure is kept constant at 12 kPa, as shown in Fig. 15(d). In summary, Fig. 15(e) reports that the average force of  $f_1$  and  $f_2$  from three trials is 0.27 N and 0.21 N, while the averaged peak values for both sensors are 0.56 N and 0.60 N, respectively. The standard deviations of the measured forces are between 0.013 ~ 0.025 N.

Fig. 16(b) shows that when operating the robot, maximum

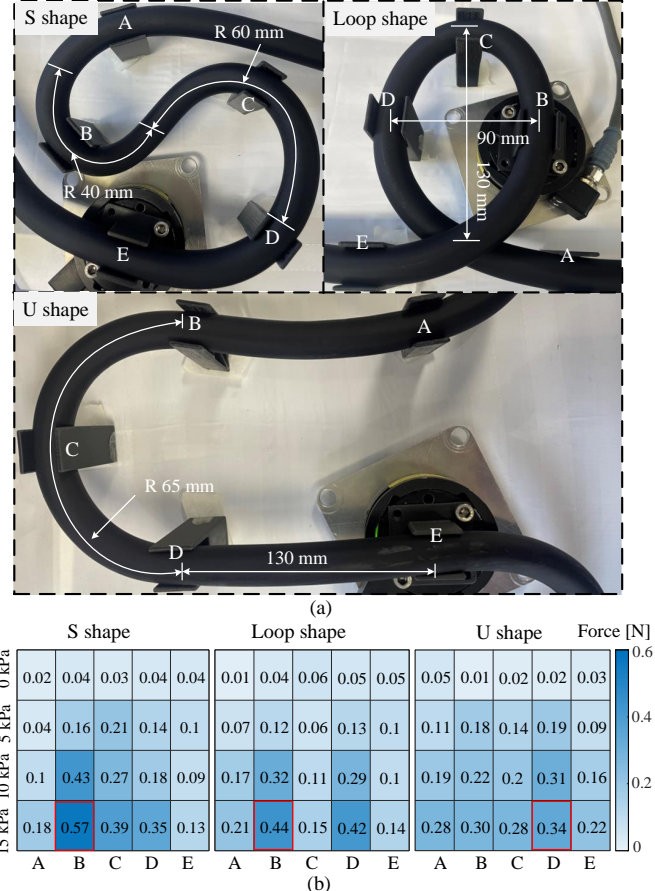


Fig. 14. Results for Experiment 2 - Static forces to preserve (a) different shapes, i.e., an S shape, a loop shape and an U shape, of the evertor robot. (b) Identified forces at five different positions with different growth pressure.

forces from two sensors are 0.70 N ( $f_{r1}$ ) and 0.65 N ( $f_{r2}$ ), respectively. In contrast, maximum force values reach 12.50 N ( $f_{s1}$ ) and 5.81 N ( $f_{s2}$ ) when advancing the conventional colonoscope. Additionally, Fig. 16(c) further reports force distributions, with mean values indicated. Specifically, the robot produces mean forces below 0.25 N, while the colonoscope generates mean forces of 3.40 N and 1.58 N, respectively. The time required to pass the phantom is approximately 70 ~ 80 seconds for the robot and 35 ~ 40 seconds for the colonoscope. For the traditional colonoscope, the NASA-TLX scores were: 80 (mental demand, low to high), 20 (physical demand, low to high), 55 (temporal demand, low to high), 80 (performance, perfect to failure), 85 (effort, low to high), and 55 (frustration, low to high). For the evertor robot, the corresponding scores were 60, 65, 50, 85, 90, and 50, respectively.

### C. Experiment 3 - Path-following in a Rigid S Shape Phantom

1) Protocol: Based on the algorithm presented in Section IV-B1, the robot was controlled to autonomously navigate through the rigid S shape phantom via the proposed closed-loop adaptive controller. This experiment was repeated three times. The desired path was defined as the middle curve of the phantom. An EM sensor was mounted at the center of

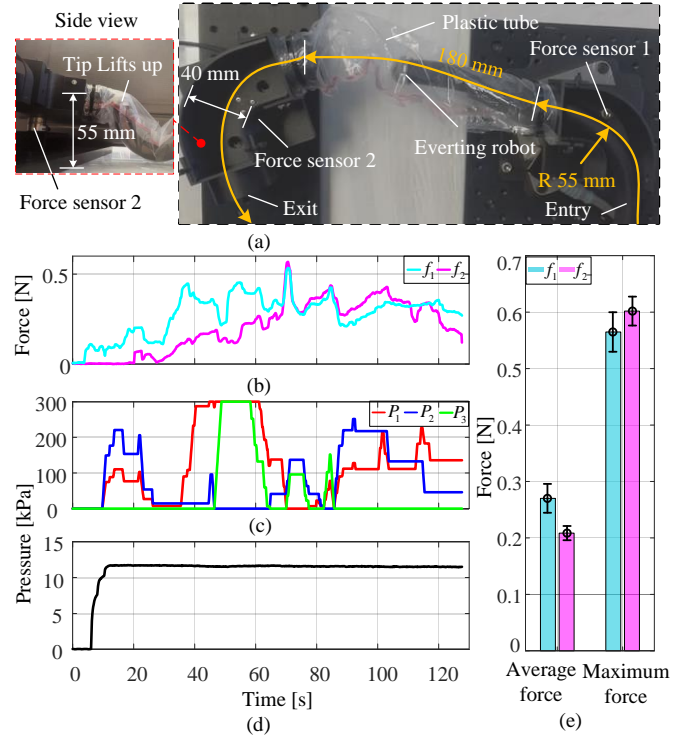


Fig. 15. Results for Experiment 2 - Interaction forces when the robot passes through (a) a phantom comprising two rigid corners connected by a plastic tube; (b) the measured interaction forces  $f_1$  and  $f_2$  at the two rigid corners; (c) the steering pressure of the tip manipulator; (d) the growth pressure from one trial; (e) The average and peak forces measured by the two sensors.

the robot's cap and measured its real-time tip position and orientation (see Fig. 17(a)). During the experiment, the motor speed  $\omega_1$  was set at a constant value of 30 RPM. The path-following adaptive control parameters were set as follows:  $\Gamma = 1 \times 10^{-4} I$ ,  $Q = \text{diag}(0.05, 1)$ ,  $\gamma = 10$ . The anti-windup integrator saturation limits were empirically set as  $|\hat{\theta}_1| \leq 3$ ,  $|\hat{\theta}_2| \leq 3$ , and  $|P_x| \leq 259.8$  kPa. The experimental setup is reported in Fig. 17(a).

2) Results: Fig. 17(a) shows the robot autonomously advancing in the S shape phantom and reports real trajectories collected from three trials. The robot can consistently follow the desired trajectory highlighted in the dash line. Specifically, the left side of Fig. 17(b) presents the mean tracking error (solid line) and standard deviation (shaded area) across three trials. The right side of Fig. 17(b) reports that mean position errors in three trials (i.e., 2.40 mm, 2.65 mm and 3.30 mm). In addition, the corresponding standard deviations are 2.02 mm, 2.15 mm and 1.98 mm, respectively. Fig. 17(c) reports the steering pressure in one trial. During 0 ~ 46.9 s, the robot passes the first bend by actuating  $P_1$  and  $P_3$ . At 46.9 s, the robot starts to enter the second bend with an opposite curve, and all steering pressure become zero. During 46.9 ~ 71.5 s, the robot travels through the second bend by modulating  $P_1$  and  $P_2$ .

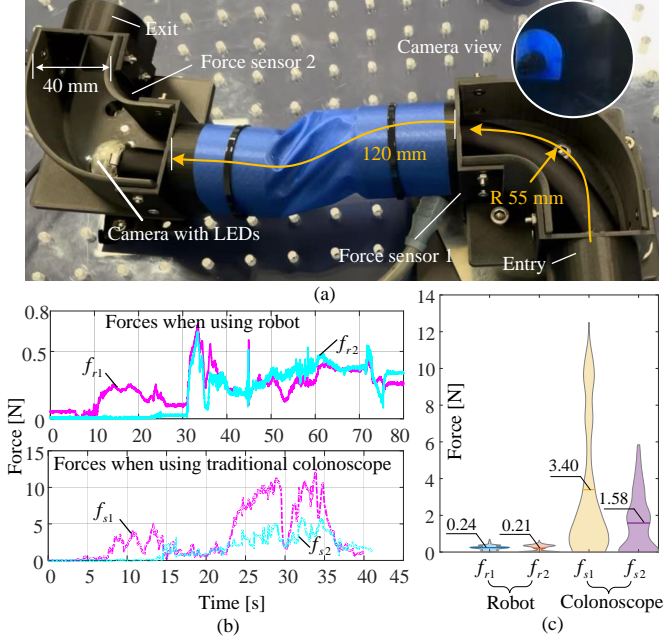


Fig. 16. Results for Experiment 2 - Comparison of interaction forces between the evertng robot and a conventional colonoscope, both operated by the same colonoscopist. (a) Experimental setup. (b) Forces recorded when operating the robot and the colonoscope. (c) Summary of force distributions plotted in violin plots, with mean values indicated.

#### D. Experiment 4 - Vision-based Locomotion in a Soft Colon Phantom

1) *Protocol:* An on-board camera [MD-V1000LH-50, MISUMI] with a better lighting performance was mounted on the tip cap. Constrained by camera's cable length, the start and the end navigation points are set in Fig. 18(a). The soft colon phantom was arranged in a semicircle with a radius of about 120 mm. During the navigation, the growth pressure was set to 12 ~ 15 kPa, and the motor speed  $\omega_1$  was set to 30 RPM when the growth was enabled. The threshold  $r$  was empirically defined as 50 pixels. The autonomous vision-based navigation was based on the control strategy presented in Section IV-B2. To further evaluate the robot's ability to follow curved trajectories using center tracking mode, we systematically varied the phantom's radius of curvature to 50 mm, 80 mm, and 100 mm, aiming to determine the minimum radius at which the robot can successfully pass. Additionally, the LED light intensity at the camera was adjusted from 0% to 100% to assess the effect of illumination on the lumen detection algorithm.

2) *Results:* Fig. 18(b) shows camera images corresponding to the two modes of operation. Combining Fig. 18(c) with Fig. 18(d), it is observed that the motor command is only enabled in the growing mode, with a constant motor speed of 30 RPM (see Fig. 18(d)). In this case,  $C_x$  and  $C_y$  are both within the defined circle (see Fig. 10) with a radius of 50 pixels. Fig. 18(e) shows the steering pressure: in the first 40 s, the controller is in the center-tracking mode, where  $P_1$  and  $P_2$  are continuously adjusted to steer the robot to the center of the detected lumen. In comparison, when the controller enters the growing mode, the steering pressures remain constant,

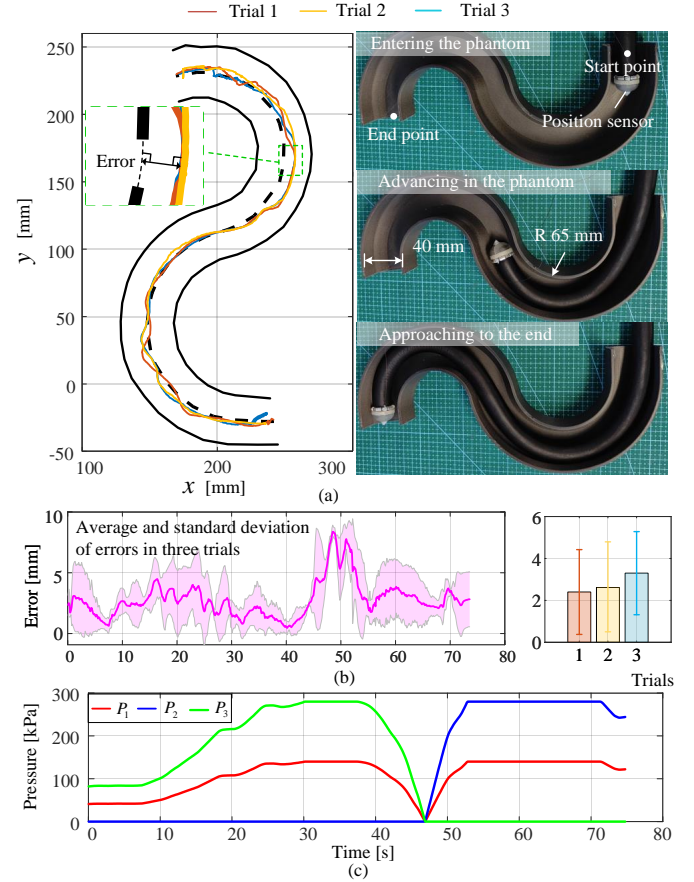


Fig. 17. Results for Experiment 3 - (a) Autonomous trajectory following control in the rigid S shape phantom. The tracking error is defined as the minimum distance between the measured position and the desired path. (b) The average and standard deviation of tracking errors across three trials (left), with the results from each trial displayed in a bar-chart (right). (c) Control pressure of the tip manipulator in one trial. One trial from this experiment is also included in the Supplementary Material.

resulting in the robot growing with a fixed steering angle. Supplementary Video further reports details of this experiment. In the additional evaluation of the autonomous navigation in the phantom with varying radii (see Fig. 19(a)), the robot successfully navigates through phantom's radius of curvature of 80 mm and 100 mm. At a radius of 50 mm, however, even at maximum steering pressure, the robot is unable to maintain its tip at the center of the detected lumen along the curve. Varying the LED light intensity revealed that lumen detection is effective starting from 20%, with higher intensities further improving the focus and localization of the detected lumen position as show in Fig. 19(b).

## VI. DISCUSSIONS AND FUTURE WORK

### A. Robot Locomotion

Experiment 1 demonstrates that the growth pressure in Fig. 13(c) when navigating in a soft colon phantom is higher than that in Fig. 11(c) when navigating in a rigid phantom. For instance, the peak growth pressure is about 18 kPa in Fig. 11(c) when the robot passes a narrow bend. This is due to the fact that the rigid phantom has a smooth surface, instead,

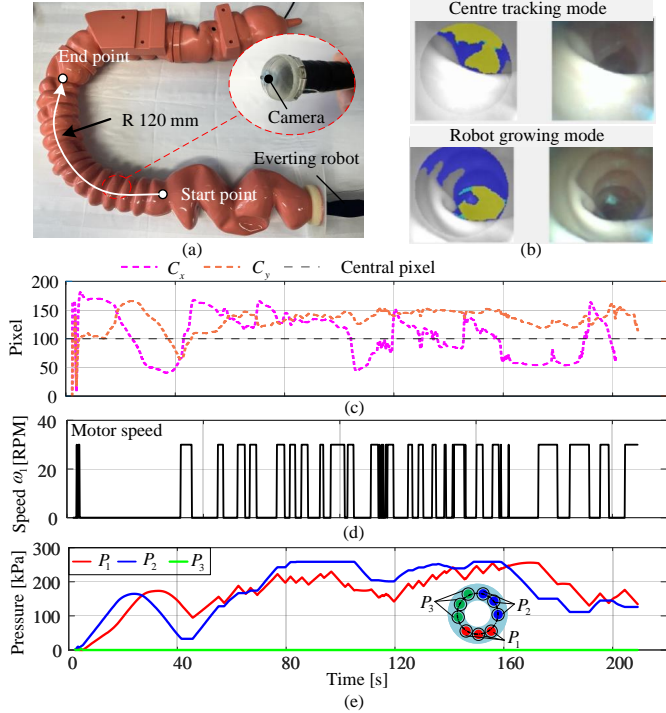


Fig. 18. Results for Experiment 4 - Vision-based navigation in the colon phantom. (a) Experimental setup, and (b) images from the tip-mounted camera and image processing according to the SfS technique. (c) Calculated lumen centroid  $C_x$  and  $C_y$  using (11) and (d) motor speed command. (e) Steering pressures of the tip manipulator.

the soft colon phantom has a corrugated structure, requiring additional pushing force to advance the robot. Even though eversion does not rely on friction with the environment, the cap slides on the phantom surface, indicating that a low-friction coating could be beneficial. In this case, the camera view helps the user trying to keep the robot tip in the center. Experiment 1 shows the locomotion capability of the robot in 3D constrained spaces.

Our evertng robot features a diameter of 18 mm and a flexible tip steering structure (see Fig. 3). A large omnidirectional steering angle over 180° is achieved in our design. Higher growth pressures increase the stiffness of the evertng structure and reduce the maximum tip steering angle [42]. In other tip steering mechanisms, the maximum achieved steering angle is 67.4° (2D) using a cable-driven rigid joint [26], 115° (2D) by a motorized revolute joint [43], 120° (3D) [27] or 106.8° [28] (3D) by two-segment pneumatic actuators [44]. It is noteworthy that the steering performance of our robot also outperforms other evertng robots steered by multiple distributed pneumatic actuators [44]. Specifically, it is reported that the maximum steering angle is between 0.5°/cm and 2.6°/cm [29]. In comparison, the achieved steering performance of our robot exceeds 12°/cm.

Table II further summarizes the steering performance of various growing robots. Our design achieves the smallest steering radius in 3D space while employing a silicone-cast, pneumatically driven soft actuator. Our approach offers several advantages, including a cost-effective alternative to [30], which depends on external magnetic field generation,

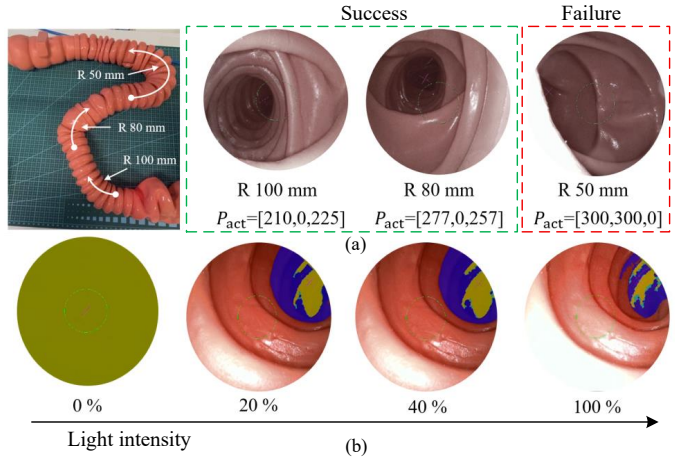


Fig. 19. Results for Experiment 4 - Vision-based navigation in the colon phantom with varying radii. (a) Experimental setup. (b) Lumen detection with varying light intensities.

and a lightweight solution compared to [45], which requires tip-mounted motors. Both our work and [27] employ pneumatically driven soft actuators for steering; however, the designs differ significantly. The mechanism in [27] consists of two 3D-printed pneumatic actuators connected in series, each with three actuation chambers. In contrast, our robot is composed of compliant silicone and features nine actuation chambers arranged in groups of three. As a result, our design achieves a steering radius approximately five times smaller than that reported in [27].

### B. Contact Force

Experiment 2 indicates that our evertng robot can conform to the shape constrained by the environment without exerting high forces, e.g., the maximum contact forces are about 0.5 N (see Fig. 14(b)). This is credited to the compliant and stretchable fabric tube, resulting a wrinkle-free curve when the robot bends [46], [47]. As such, no additional shape-locking mechanisms, such as hook-and-loop fasteners [48] and magnetic valves [29], are required. This passive shape-locking property is particularly important for the colonoscopy. According to results from [6] and Experiment 2 (see Fig. 16), the exerted forces by traditional colonoscopes can reach 12.50 ~ 12.73 N. In contrast, our robot generates forces that are 10 times lower, remaining below 1 N. The contact force of our robot is comparable to, if not better than, other recently developed robotic colonoscopes, such as those in [9] and [3], with peak contact forces lower than 1 ~ 2 N. Moreover, our robotic system achieves tip growth based on the evertng principle, eliminating the need to insert the device. This will prevent the colon from forming loops when the device advances [7], which could further reduce pain for patients. As a result, the proposed system could reduce patient discomfort associated to colonoscopies.

### C. Modes of Operation

The NASA-TLX assessment in Experiment 2 demonstrates that the evertng robot is less mentally demanding than the

TABLE II  
COMPARISON OF ACTIVE STEERING RADIUS

Reference	Steering Principle	Steering Radius (cm)	Steering Space
[26]	Tip cable-driven actuator	$\approx 12.2$	2D
[27]	Tip pneumatic printed actuator	$\leq 20$	3D
[30]	Tip magnet	$6.7 \sim 7.2$	2D
	Distributed cPAM*	$\approx 22$	2D
[44]	Distributed pouch motor	$\approx 52$	2D
	Distributed fPAM*	$\approx 95$	2D
[45]	Tip cable-driven actuator	$< 6.0$	2D
This work	Tip pneumatic soft actuator	$\leq 4.8$	3D

\* cylindrical pneumatic artificial muscle (cPAM); fabric pneumatic artificial muscle (fPAM).

conventional scope, suggesting its potential to shorten the learning curve. However, it appears to require greater physical demand on the colonoscopist, which may be attributed to limited practice with the device. In terms of temporal demand, required effort, and frustration levels, the robotic scope shows performance comparable to that of the traditional colonoscope. Please note that above data is from one user, which cannot fully represent the broader population of endoscopists. Additionally, more comprehensive usability evaluation of the evertting robot was conducted in an operation room, involving nine experienced endoscopists [49]. The results highlight that the robotic device is perceived as easy to use (8.11/10, “Extremely agree”) and has significant potential to advance endoscopic technologies (8.33/10, “Extremely agree”).

Fig. 17(b) shows that tracking errors increase when the robot transitions from the first bend to the second bend in the S shape phantom, due to the fact that the tip steering mechanism cannot generate two opposite bending curvature at the same time. Please note that position errors are measured when the robot navigates in confined spaces. As such, maximum position control errors might be reduced resulting from the wall constraints. In our setup, the rigid phantom has a width of 40 mm, which implies a maximum acceptable position error of approximately 10 mm (see Fig. 17(a)). This aligns with the results shown in Fig. 17(b), where a maximum error of 9.44 mm is observed. In the future, alternative metrics for evaluating and enhancing controller performance could incorporate both absolute position errors and dimensions of spatial constraints of the environment. Experiments 3 and 4 demonstrate that the robot can achieve autonomous locomotion, either following known predefined trajectories or navigating within an unknown colon phantom using real-time camera perception. Fig. 17(b) illustrates that the average time to navigate the S shape phantom in autonomous fashion is about 73.2 s. This is similar to the reported time (i.e., 71.5 s), when experienced users employed the teleoperation mode (see Fig. 11). It is worth mentioning that the required time is expected to be longer when new users teleoperate the robot. By comparing Fig. 18 with Fig. 13, the results show that the robot’s advancing speed in the soft colon phantom using the vision-based autonomous mode is approximately 3 ~ 4 times slower than in the teleoperation mode. This is primarily due

TABLE III  
CAPABILITY COMPARISON BETWEEN OUR ROBOT AND THE OLYMPUS CF-H260AZL

Comparisons	Our evertting robot	Olympus CF-H260AZL
Diameter	18 mm	12.9 mm
Working length	1.6 m	1.68 m
Steering curvature	$\leq 4.8$ cm	$\leq 3.5$ cm
Maximum contact forces	0.70 N	12.50 N
Operation time *	70 ~ 80 seconds	35 ~ 40 seconds

\* The robot’s operation time was performed by a new colonoscopist. In the future, this time could be further reduced by increasing the motor speed and providing more comprehensive user training.

to the small value of the integral gain parameter  $k_i$  and the threshold value of  $r$  in (12) which was employed to ensure a smooth steering adjustment. In addition, the supplementary video shows that the robot tip hits the colon phantom three times when manually controlled with the joystick, while it does not hit the phantom and stays in the center of the lumen in the vision-based autonomous mode.

Compared to other new colonoscopes [3], [9], [11], this work for the first time demonstrates that the evertting robot can achieve autonomous locomotion in a soft colon phantom. Compared to magnetically actuated scopes [4], [12], our robot operates with an external pressure of 3 bar and does not require external magnetic fields or specialized facilities. Most operating rooms are equipped with pressurized air supply (e.g., up to 4 bar) for powering ventilators and surgical tools. This makes our solution more accessible, cost-effective, and easier to integrate into existing medical environments. As highlighted in [1], the level of autonomy of medical robots is categorized into six levels. For instance, The Endotics colonoscope in [9] is teleoperated using a joystick, advancing the autonomy level of colonoscopy from no autonomy to robot assistance. Our device supports both teleportation by joysticks and autonomous operation via sensor perception, further advancing the level to task autonomy.

#### D. Robot Design

This work presents a soft evertting robot with potential for colonoscopy, but there are a few limitations to consider, including its diameter and steering curvature, as outlined in Table III. Since the steering tip manipulator and the growing tube of the robot are fabricated in our lab, miniaturization is possible in principle (e.g., reaching an outer diameter of 10 mm is realistic [51]). However, the outer diameter is constrained by the central working channel, which must accommodate the evertting material and future therapeutic tools. Current designs, with a 16.9 mm outer diameter and 7.9 mm lumen, suggest a feasible minimum robot’s diameter of 13–15 mm, with a working channel of 5 ~ 6 mm.

Steering capability is influenced by both actuation and growth pressures (see Fig. 6). Higher growth pressure stiffens the growing structure, limiting the curvature of the steering manipulator. Reducing the steering radius may require increasing the stiffness of the steering manipulator, potentially

TABLE IV  
COMPARISON OF OUR SOFT EVERTING ROBOT WITH EXISTING WORKS ON COLONOSCOPY UTILIZING THE GROWING PRINCIPLE

Reference	Tube Diameter	Steering Principle of Growing robots	Steering Capability	Shape-holding Capability	Contact Force Identification	Path-following Navigation	Vision-based Navigation
[17]*	25.4 ~ 50.8 mm	No active steering	–	Passively held	Mean $\approx$ 2 ~ 10 N**	No	No
[19]	Varying, < 38 mm	No active steering	–	Passively held	No	No	No
[30]	25 mm	Tip magnet	$\approx 9^\circ/\text{cm}$	Passively held	No	No	No
[50]	27 mm	Crawling pneumatic soft manipulator	$\approx 10^\circ/\text{cm}$	Passively held	No	No	No
This work	18 mm	Tip pneumatic soft manipulator	$\geq 12^\circ/\text{cm}$	Passively held	Mean $\leq 0.3 \text{ N}$ **	Yes	Yes

\* Traditional colonoscopes are required to be attached inside the evertng structure in [17].

\*\* The mean insertion force in [17] is about 10 N when the radius of the phantom is 76.2 mm. Our force is measured with a phantom radius of 55 mm.

raising the actuation pressure. Additional testing is required to optimize steering performance based on curvature and material properties.

Regarding the robot's growth length, while it can extend to 1.6 m for colonoscopy, friction and tighter bends in confined spaces like the small intestine may pose challenges in achieving a longer length. The small intestine also requires a narrower diameter ( $\approx 10 \text{ mm}$ ), presenting challenges for the current design. Adapting the growing robot for the small intestine is an exciting direction, but is beyond the scope of this study.

#### E. Future Work

As highlighted in Table IV, this work makes significant advancements in robotic colonoscopes employing the evertng principle, particularly in terms of size miniaturization, active steering capabilities, quantitative analysis of interaction forces, and autonomous operation. However, there remain several areas for potential improvement in future work. As demonstrated in Fig. 18, the camera cable runs outside of the evertng structure. In future work, we will explore approaches to provide access to the central working channels of the evertng robot, allowing the integration of medical tools. Theoretical models will be investigated to describe growth, steering and force characteristics in order to generate design guidelines. Since the robot grows by eversion and steers by a soft continuum manipulator, the contact-aided motion planning [52] and Cosserat rod model [42] might be applicable. The autonomous control pipeline presented in Section IV-B highlights the autonomy level of the robot, but its performance can be improved. For instance, the advancing speed in the vision-based control mode can be increased by optimizing control parameters or exploring other advanced lumen detection and motion planning techniques [53], such as reinforcement learning-based method [54]. In addition, the current center-tracking approach cannot maintain lumen alignment when the required curvature exceeds the robot's maximum bend, highlighting the need for alternative motion planning and adaptive steering to navigate highly curved environments.

It must be noted that this work focuses on the forward motion of the robotic device. Once it has traversed the full length of the colon, the device can be manually retracted while the camera-equipped tip can be oriented using the tip steering manipulator to screen the colon. This approach aligns with

standard colonoscopy procedures, where most examinations occur during scope retraction. Due to the high compliance of the fabric tube, buckling effect prevents the current system from achieving fully automated retraction. Tip retraction mechanisms can be explored in the future, which could further enhance the system's performance. Finally, extensive *in-vivo* experiments are required to assess the performance of the system in more realistic clinical settings.

We selected silicone/polyurethane-coated nylon fabric for the growing structure due to its potential biocompatibility. While the current material has not yet received formal medical approval, existing evidence suggests its suitability for biomedical applications. Specifically, silicone and polyurethane are highly biocompatible and bio-durable when interacting with tissues [55] and are extensively used in various medical devices, including urinary catheters, nerve conduits, and heart valves [56]. Additionally, nylon is recognized for its chemical stability and biocompatibility, making it a common material for sutures and catheters [57]. In the future, further biocompatibility assessments, such as irritation and toxicity testing, should be conducted in accordance with medical device standards, such as ISO 10993, to ensure its safety and regulatory compliance.

## VII. CONCLUSION

This paper presented a novel soft evertng robot for colonoscopy. This soft robotic device features agile omnidirectional tip steering over  $180^\circ$ , with an 18 mm tube structure and a growth length of 1.6 m. Detailed descriptions of the hardware design, fabrication process, and control algorithms were provided. Comprehensive experimental evaluations in *in-vitro* environments validated the robot's functionality and feasibility. The robot achieves tip growth through the eversion principle, eliminating the need for insertion during advancement and maintaining low contact forces, averaging less than 0.3 N. The robot can operate in two modes: teleoperation using joystick, and autonomous navigation, based on sensor inputs. In autonomous mode, it was capable of both following predefined paths using a closed-loop adaptive controller and navigating in an unknown soft colon phantom using image-guidance from a tip-mounted camera. These validation results highlight the robot's potential to enhance the safety and autonomy level of colonoscopy procedures.

## APPENDIX A

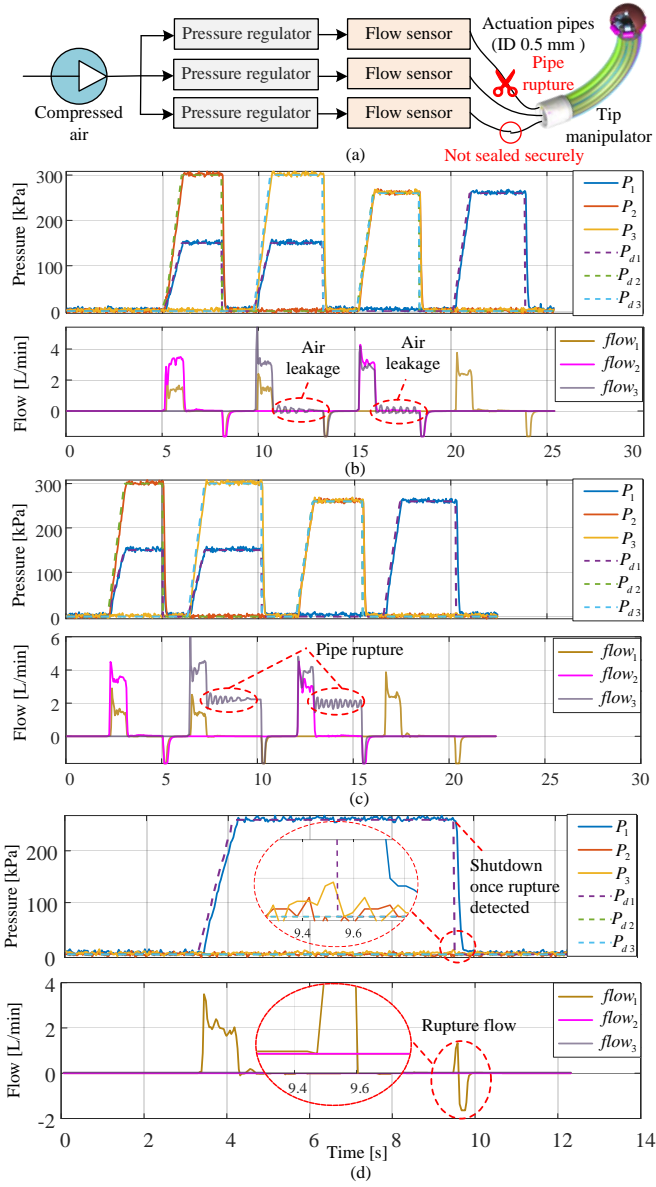


Fig. 20. Safety assessment of the steering manipulator. (a) Test setup with two failure modes: pipe rupture and air leakage. Detection of (b) air leakage and (c) pipe rupture with monitored air flow. (d) Demonstration of pressure response after detected pipe rupture.

#### SAFETY ASSESSMENT OF ACTUATION PRESSURES

As reported in [58], the rupture pressure of the human cadaver colon ranges from 10 to 20 kPa, depending on the specific section. In contrast, our system operates with a steering pressure of up to 300 kPa, which could pose potential risks to the colon subject to unexpected system failures, such as rupture or air leakage. Safety of the robot can be ensured by incorporating flow sensors to monitor both the growing and steering pressure. If abnormal airflow is detected, the system can immediately shut off the actuation pressure to prevent hazards. To demonstrate the safety assessment of the operation pressure, Fig. 20(a) illustrates the integration of three flow sensors [SENSIRION, SFM4300] positioned between the pressure regulators and the actuation pipes (length of 1.6 m,

ID of 0.5 mm) of the steering manipulator.

#### A. Leakage and Rupture Detection

Two failure modes were assessed: pipe rupture and leakage. The rupture was simulated by cutting the actuation pipe directly and the leakage was simulated by loosely sealing pipe connections. In both cases, three chambers were actuated by steering the manipulator in the order of up→down→left→right. The desired pressure, actual pressure, and airflow were recorded throughout the process.

Fig. 20(b) presents the results of leakage detection. The data indicate that airflow is not zero in all three chambers when the command pressure varies.  $flow_3$  fluctuates around zero while maintaining  $P_3$  as a nonzero constant, whereas  $flow_1$  and  $flow_2$  drop to zero when  $P_1$  and  $P_2$  are held at non-zero constants. The fluctuation of  $P_3$  suggests that the pressure regulator continuously compensates for air loss to stabilize the pressure as leakage exists. Fig. 20(c) illustrates rupture detection. Here,  $flow_3$  fluctuates around 2 L/min when the desired pressure remains constant, while  $flow_1$  and  $flow_2$  reset to zero when  $P_1$  and  $P_2$  are held at non-zero constants.

#### B. Pressure Shutoff after Detected Rupture

Upon detection of a failure, the system can actively shut off the pressure to ensure safety. To demonstrate this, we actuated  $P_1$  to 300 kPa, then simulated a pipe rupture by cutting the pipe with a scissor between 9 ~ 10 seconds. Pressure and flow data were recorded throughout the process.

Fig. 20(d) shows that  $P_1$  decreases to zero within a time duration  $t_l$  of 150 ms, and the maximum value of  $flow_2$  is 1.3 L/min. Assuming the rupture occurs in the colon, the estimation of the colon pressure variation can follow:

$$P_1(t_l) \int_0^{t_l} flow_1(t) dt = \Delta P_c V_c < P_{1,max} \int_0^{t_l} flow_{1,max} dt, \quad (13)$$

where  $\Delta P_c$  and  $V_c$  are the colon pressure variation and the colon volume, respectively. To provide a conservative estimation of  $\Delta P_c$ , the maximum values of  $P_1$  and  $flow_1$ , and  $t_l$  of 150 ms are substituted into (13).  $\Delta P$  is then calculated to be less than 0.5 kPa. Therefore, the safety can be ensured by incorporating the rupture detection feature in future systems. In practice, the leaked air from the steering manipulator goes into the evertting tube instead of the colon. Notably, [34] demonstrates that the rupture pressure of a silicone-coated fabric tube exceeds 300 kPa, while our typical growth pressure remains below 15 kPa. This indicates that colon rupture is fully prevented in our system. Furthermore, leakage detection of the growth tube can be implemented by integrating another flow sensor, which we will include in the next step.

#### ACKNOWLEDGMENT

For the purpose of open access, the author has applied a Creative Commons Attribution (CC BY) license to any Author Accepted Manuscript version arising. The authors would like to thank the colonoscopist, Ahmed Jabed, for his valuable support in conducting the force comparison experiments between the robot and the conventional colonoscope.

## REFERENCES

- [1] G.-Z. Yang *et al.*, "Medical robotics—regulatory, ethical, and legal considerations for increasing levels of autonomy," *Sci. Rob.*, vol. 2, no. 4, p. eaam8638, 2017.
- [2] M. Yip *et al.*, "Artificial intelligence meets medical robotics," *Science*, vol. 381, no. 6654, pp. 141–146, 2023.
- [3] J. E. Bernth *et al.*, "MorphGI: A self-propelling soft robotic endoscope through morphing shape," *Soft Rob.*, vol. 11, no. 4, pp. 670–683, 2024.
- [4] J. W. Martin *et al.*, "Enabling the future of colonoscopy with intelligent and autonomous magnetic manipulation," *Nat. Mach. Intell.*, vol. 2, no. 10, pp. 595–606, 2020.
- [5] G. Ciuti *et al.*, "Frontiers of robotic colonoscopy: A comprehensive review of robotic colonoscopes and technologies," *J. Clin. Med.*, vol. 9, no. 6, p. 1648, 2020.
- [6] S. Dogramadzi, G. Virk, G. Bell, R. Rowland, and J. Hancock, "Recording forces exerted on the bowel wall during colonoscopy: in vitro evaluation," *Int. J. Med. Robot. Comput. Assist. Surg.*, vol. 1, no. 4, pp. 89–97, 2005.
- [7] A. J. Loeve, P. Fockens, and P. Breedveld, "Mechanical analysis of insertion problems and pain during colonoscopy: Why highly skill-dependent colonoscopy routines are necessary in the first place... and how they may be avoided," *Can. J. Gastroenterol. Hepatol.*, vol. 27, no. 5, pp. 293–302, 2013.
- [8] D. R. Kohli and J. Baillie, "3 - How endoscopes work," in *Clinical Gastrointestinal Endoscopy (Third Edition)*. Philadelphia: Elsevier, 2019, pp. 24–31.
- [9] F. Cosentino, E. Tumino, G. R. Passoni, E. Morandi, and A. Capria, "Functional evaluation of the endotaxis system, a new disposable self-propelled robotic colonoscope: in vitro tests and clinical trial," *Int. J. Artif. Organs*, vol. 32, no. 8, pp. 517–527, 2009.
- [10] L. Manfredi, E. Capoccia, G. Ciuti, and A. Cuschieri, "A soft pneumatic inchworm double balloon (SPID) for colonoscopy," *Sci. Rep.*, vol. 9, no. 1, p. 11109, 2019.
- [11] T. T. Nguyen, D. Q. Nguyen, and V. A. Ho, "Soft robot employing a series of pneumatic actuators and distributed balloons: Modeling, evaluation, and applications," *IEEE Trans. Robot.*, vol. 40, pp. 3933–3949, 2024.
- [12] X. Yu, J. Wang, J. Su, and S. Song, "Inchworm-like biomimetic magnetic-driven robotic shell for capsule endoscope in a tubular environment," *IEEE/ASME Trans. Mechatronics*, pp. 1–11, 2024.
- [13] X. Dray *et al.*, "Artificial intelligence in small bowel capsule endoscopy—current status, challenges and future promise," *J. Gastroenterol. Hepatol.*, vol. 36, no. 1, pp. 12–19, 2021.
- [14] M. M. Coad *et al.*, "Vine robots," *IEEE Robot. Autom. Mag.*, vol. 27, no. 3, pp. 120–132, 2020.
- [15] E. W. Hawkes, L. H. Blumenschein, J. D. Greer, and A. M. Okamura, "A soft robot that navigates its environment through growth," *Sci. Rob.*, vol. 2, no. 8, p. eaan3028, 2017.
- [16] K. Borvorntanajanya, S. Treratanakulchai, F. R. y. Rodriguez, and E. Franco, "Model-based tracking control of a soft growing robot for colonoscopy," *IEEE Trans. Med. Robot. Bionics.*, vol. 6, no. 4, pp. 1354–1362, 2024.
- [17] A. Saxena, E. M. Pauli, R. S. Haluck, B. Fell, and J. Moore, "Tubular Locomotion and Positioning Using Tip Eversion for Endoscopy," *J. Mech. Des.*, vol. 14, no. 2, p. 021004, 03 2020.
- [18] P. Berthet-Rayne *et al.*, "Mammobot: A miniature steerable soft growing robot for early breast cancer detection," *IEEE Trans. Robot. Autom.*, vol. 6, no. 3, pp. 5056–5063, 2021.
- [19] H. Dehghani *et al.*, "Design and preliminary evaluation of a self-steering, pneumatically driven colonoscopy robot," *J. Med. Eng. Technol.*, vol. 41, no. 3, pp. 223–236, 2017.
- [20] L. H. Blumenschein, M. M. Coad, D. A. Haggerty, A. M. Okamura, and E. W. Hawkes, "Design, modeling, control, and application of evertive vine robots," *Front. Rob. AI*, vol. 7, p. 548266, 2020.
- [21] J. D. Greer, T. K. Morimoto, A. M. Okamura, and E. W. Hawkes, "A soft, steerable continuum robot that grows via tip extension," *Soft Rob.*, vol. 6, no. 1, pp. 95–108, 2019.
- [22] N. D. Naclerio *et al.*, "Controlling subterranean forces enables a fast, steerable, burrowing soft robot," *Sci. Rob.*, vol. 6, no. 55, p. eabe2922, 2021.
- [23] Y. Satake, A. Takanishi, and H. Ishii, "Novel growing robot with inflatable structure and heat-welding rotation mechanism," *IEEE/ASME Trans. Mechatronics*, vol. 25, no. 4, pp. 1869–1877, 2020.
- [24] J. D. Greer, L. H. Blumenschein, R. Alterovitz, E. W. Hawkes, and A. M. Okamura, "Robust navigation of a soft growing robot by exploiting contact with the environment," *Int. J. Rob. Res.*, vol. 39, no. 14, pp. 1724–1738, 2020.
- [25] C. Girerd, A. Alvarez, E. W. Hawkes, and T. K. Morimoto, "Material scrunching enables working channels in miniaturized vine-inspired robots," *IEEE Trans. Robot.*, vol. 40, pp. 2166–2180, 2024.
- [26] T. Takahashi *et al.*, "Eversion robotic mechanism with hydraulic skeleton to realize steering function," *IEEE Trans. Robot. Autom.*, vol. 6, no. 3, pp. 5413–5420, 2021.
- [27] P. A. der Maur *et al.*, "Roboa: Construction and evaluation of a steerable vine robot for search and rescue applications," in *Proc. IEEE Int. Conf. Soft Robot.*, 2021, pp. 15–20.
- [28] T. Wen *et al.*, "Design, performance analysis, and experiments of a soft robot for rescue," *J. Mech. Rob.*, vol. 16, no. 7, 2024.
- [29] A. M. Kübler *et al.*, "A multi-segment, soft growing robot with selective steering," in *Proc. IEEE Int. Conf. Soft Robot.*, 2023, pp. 1–7.
- [30] N. G. Kim *et al.*, "External steering of vine robots via magnetic actuation," *Soft Rob.*, pp. 1–12, 2024.
- [31] J. Davy *et al.*, "Vine robots with magnetic skin for surgical navigations," *IEEE Trans. Robot. Autom.*, vol. 9, no. 8, pp. 6888–6895, 2024.
- [32] A. Alazmani, A. Hood, D. Jayne, A. Neville, and P. Culmer, "Quantitative assessment of colorectal morphology: Implications for robotic colonoscopy," *Med. Eng. Phys.*, vol. 38, no. 2, pp. 148–154, 2016.
- [33] J. Wehrmeyer, J. Barthel, J. Roth, and T. Saifuddin, "Colonoscope flexural rigidity measurement," *Med. Biol. Eng. Comput.*, vol. 36, pp. 475–479, 1998.
- [34] N. D. Naclerio and E. W. Hawkes, "Simple, low-hysteresis, foldable, fabric pneumatic artificial muscle," *IEEE Trans. Robot. Autom.*, vol. 5, no. 2, pp. 3406–3413, 2020.
- [35] S.-G. Jeong *et al.*, "A tip mount for transporting sensors and tools using soft growing robots," in *Proc. IEEE/RSJ Int. Conf. Intell. Robots Syst.*, 2020, pp. 8781–8788.
- [36] J. Shi, S.-A. Abad, J. S. Dai, and H. A. Wurdemann, "Position and orientation control for hyperelastic multisegment continuum robots," *IEEE/ASME Trans. Mechatronics*, vol. 29, no. 2, pp. 995–1006, 2024.
- [37] J. Shi, G. Shi, Y. Wu, and H. A. Wurdemann, "A multi-cavity touch interface for a flexible soft laparoscopy device: Design and evaluation," *IEEE Trans. Med. Robot. Bionics.*, vol. 6, no. 4, pp. 1309–1321, 2024.
- [38] K. Chen and A. Astolfi, "On the adaptive tracking problem of time-varying systems using the congelation for variables method," *IFAC-PapersOnLine*, vol. 56, no. 1, pp. 13–18, 2023.
- [39] H. Chettaoui, G. Thomann, C. B. Amar, and T. Redarce, "Extracting and tracking colon's "pattern" from colonoscopic images," in *Can. Conf. Comput. Robot. Vis.*, 2006, pp. 65–65.
- [40] Z. Wu, S. M. H. Sadati, K. Rhode, and C. Bergeles, "Vision-based autonomous steering of a miniature eversion growing robot," *IEEE Trans. Robot. Autom.*, vol. 8, no. 11, pp. 7841–7848, 2023.
- [41] B. Bhatnagar, C. Sharma, S. Gupta, M. Mathur, and D. Reddy, "Study on the anatomical dimensions of the human sigmoid colon," *Clin. Anat.*, vol. 17, no. 3, pp. 236–243, 2004.
- [42] J. Shi *et al.*, "Stiffness modelling and analysis of soft fluidic-driven robots using Lie theory," *Int. J. Rob. Res.*, vol. 43, no. 3, pp. 354–384, 2024.
- [43] D. A. Haggerty, N. D. Naclerio, and E. W. Hawkes, "Hybrid vine robot with internal steering-reeling mechanism enhances system-level capabilities," *IEEE Trans. Robot. Autom.*, vol. 6, no. 3, pp. 5437–5444, 2021.
- [44] A. M. Kübler *et al.*, "A comparison of pneumatic actuators for soft growing vine robots," *Soft Rob.*, vol. 11, no. 5, pp. 857–868, 2024.
- [45] D.-G. Lee, N. G. Kim, and J.-H. Ryu, "High-curvature consecutive tip steering of a soft growing robot for improved target reachability," in *Proc. IEEE/RSJ Int. Conf. Intell. Robots Syst.*, 2023, pp. 6477–6483.
- [46] N. G. Kim and J.-H. Ryu, "A soft growing robot using hyperelastic material," *Adv. Intell. Syst.*, vol. 5, no. 2, p. 2200264, 2023.
- [47] D. A. Haggerty, N. D. Naclerio, and E. W. Hawkes, "Characterizing environmental interactions for soft growing robots," in *Proc. IEEE/RSJ Int. Conf. Intell. Robots Syst.*, 2019, pp. 3335–3342.
- [48] R. Jitosh, S. Simón-Trench, A. M. Okamura, and B. H. Do, "Passive shape locking for multi-bend growing inflated beam robots," in *Proc. IEEE Int. Conf. Soft Robot.*, 2023, pp. 1–6.
- [49] J. F. Ahmed *et al.*, "Reducing applied force in colonoscopy using a novel soft robotic colonoscope: A head-to-head study," *Endosc. Int. Open*, 2025.
- [50] A. Giri, C. Girerd, J. Cervera-Torralba, M. T. Tolley, and T. K. Morimoto, "InchIGRAB: An inchworm-inspired guided retraction and

- bending device for vine robots during colonoscopy," *IEEE/ASME Trans. Mechatronics*, pp. 1–12, 2025.
- [51] J. Shi, S.-A. Abad, A. Menciassi, K. Althoefer, and H. A. Wurdemann, "Miniatuerised soft manipulators with reinforced actuation chambers on the sub-centimetre scale," in *Proc. IEEE Int. Conf. Soft Robot.*, 2024, pp. 157–164.
- [52] P. Rao, O. Salzman, and J. Burgner-Kahrs, "Towards contact-aided motion planning for tendon-driven continuum robots," *IEEE Trans. Robot. Autom.*, vol. 9, no. 5, pp. 4687–4694, 2024.
- [53] A. Pore, Z. Li *et al.*, "Autonomous navigation for robot-assisted intraluminal and endovascular procedures: A systematic review," *IEEE Trans. Robot.*, vol. 39, no. 4, pp. 2529–2548, 2023.
- [54] A. Pore *et al.*, "Colonoscopy navigation using end-to-end deep visuo-motor control: A user study," in *Proc. IEEE/RSJ Int. Conf. Intell. Robots Syst.*, 2022, pp. 9582–9588.
- [55] M. Zare, E. R. Ghomi, P. D. Venkatraman, and S. Ramakrishna, "Silicone-based biomaterials for biomedical applications: Antimicrobial strategies and 3D printing technologies," *J. Appl. Polym. Sci.*, vol. 138, no. 38, p. 50969, 2021.
- [56] B. Liu *et al.*, "Performance characterization and biocompatibility assessment of silicone polyurethanes for polymer heart valve applications," *RSC Adv.*, vol. 14, no. 16, pp. 10 858–10 873, 2024.
- [57] M. Shakiba *et al.*, "Nylon—A material introduction and overview for biomedical applications," *Polym. Adv. Technol.*, vol. 32, no. 9, pp. 3368–3383, 2021.
- [58] R. Kozarek, D. Earnest, M. Silverstein, and R. Smith, "Air-pressure-induced colon injury during diagnostic colonoscopy," *Gastroenterol.*, vol. 78, no. 1, pp. 7–14, 1980.



**Enrico Franco** received the M.Sc. degree in mechanical engineering from Politecnico di Torino, Torino, Italy, in 2004, and the Ph.D. degree in medical robotics from Imperial College London, London, U.K., in 2015. He is currently a Lecturer with the Hamlyn Centre for Robotic Surgery, Department of Mechanical Engineering. His research interests include medical robotics, nonlinear control, and its applications to soft robotics.



**Jialei Shi** received the B.S. degree in Naval Architecture and Ocean Engineering from the Harbin Institute of Technology, China, in 2017, and the M.S. degree in Aerospace Engineering from the Beijing Institute of Technology, China, in 2019, and the Ph.D. degree in Mechatronic and Robotic Engineering from the University College London, UK, in 2024. He is currently a Research Associate in the Hamlyn Centre for Robotic Surgery, Imperial College London. His research interests include soft robotics and medical devices.



**Ferdinando Rodriguez y Baena** (Member, IEEE) received the M.Eng. degree in mechatronics and manufacturing systems engineering from King's College London, London, U.K., in 2000, and the Ph.D. degree in medical robotics from Imperial College London, London, U.K., in 2004. He is currently a Professor of Medical Robotics with the Department of Mechanical Engineering, Imperial College London, where he leads the Mechatronics in Medicine Laboratory and the Applied Mechanics Division. He has been the Engineering CoDirector of the Hamlyn Centre for Robotic Surgery, which is part of the Institute of Global Health Innovation, since July 2020. His research interests include mechatronic systems for diagnostics, surgical training, and surgical intervention.



**Korn Borvorntanajanya** (Student Member, IEEE) is a Ph.D. student in the Mechanical Engineering Department at Imperial College London, UK. In 2018, He received an M.S. degree in Biomedical Engineering from Mahidol University, Thailand, where he also earned his B.Eng. degree in Biomedical Engineering. His research interests include bio-inspiration, soft robotics and medical robotics.



**Kaiwen Chen** (Member, IEEE) received the B.Sc. degree in electrical engineering from the University of Illinois Urbana-Champaign, IL, USA, and the B.Eng. degree in automation from the Elite Program of the Harbin Institute of Technology, Harbin, China, in 2016, the M.Sc. degree in control systems and the Ph.D. degree in nonlinear control systems from Imperial College London, London, U.K., in 2017 and 2022, respectively. He is currently a Research Associate with the Control and Power Research Group, Imperial College London. His research interests include nonlinear and adaptive control theory and its applications, with emphasis on cyber-physical-human systems and soft robotics.